

Elsevier required licence: © <2020>. This manuscript version is made available under the CC-BY-NC-ND 4.0 license <http://creativecommons.org/licenses/by-nc-nd/4.0/>
The definitive publisher version is available online at
[\[https://www.sciencedirect.com/science/article/pii/S0048969720347409?via%3Dihub\]](https://www.sciencedirect.com/science/article/pii/S0048969720347409?via%3Dihub)

Near-Field Dynamics and Plume Dispersion after an On-Road Truck: Implication to Remote Sensing

Jingwei Xie¹, Chun-Ho Liu^{1,*}, Ziwei Mo¹, Yuhan Huang^{2,3} and Wai-Chuen Mok^{1,2}

¹Department of Mechanical Engineering, The University of Hong Kong, Hong Kong

²Centre for Green Technology, School of Civil and Environmental Engineering, University of
Technology Sydney, Australia

³Jockey Club Heavy Vehicle Emission Testing and Research Centre, Vocational Training
Council, Hong Kong

Manuscript submitted

to

Science of the Total Environment

on

April 30, 2020

**Corresponding author address:*

Chun-Ho LIU

Department of Mechanical Engineering

7/F, Haking Wong Building

The University of Hong Kong

Pokfulam Road, Hong Kong, CHINA

Tel: +852 3917 7901 / +852 9788 7951

Fax: +852 2858 5415

Email: liuchunho@graduate.hku.hk

<https://aplhk.tech>

Near-Field Dynamics and Plume Dispersion after an On-Road Truck: Implication to Remote Sensing

Jingwei Xie¹, Chun-Ho Liu¹, Ziwei Mo¹, Yuhan Huang^{2,3} and Wai-Chuen Mok^{1,2}

¹Department of Mechanical Engineering, The University of Hong Kong, Hong Kong

²Centre for Green Technology, School of Civil and Environmental Engineering, University of
Technology Sydney, Australia

³Jockey Club Heavy Vehicle Emission Testing and Research Centre, Vocational Training
Council, Hong Kong

Abstract

Apart from the aerodynamic performance (efficiency and safety), the wake after an on-road vehicle substantially influences the tailpipe pollutant dispersion (environment). Remote sensing is the most practicable measure for large-scale emission source control. Its reliability, however, is largely dictated by how best the complicated vehicular flows and instrumentation constraint are tackled. Specifically, the two are the broad range of motion scales and the short sampling duration (less than 1 sec). Their impact on remote sensing has not been studied. Large-eddy simulation (LES) is thus employed in this paper to look into the dynamics and the plume dispersion after an on-road heavy-duty truck at speed U_∞ so as to elucidate the transport mechanism, examine the sampling uncertainty and develop the remedial measures. A major recirculation of size comparable to the trunk height h is induced collectively by the roof-level prevailing flows, side entrainment and underbody wall jet. The tailpipe is enclosed by dividing streamlines so the plume is carried back to the truck right after emission. The recirculation augments the pollutant mixing, resulting in a more homogeneous pollutant concentration together with a rather high fluctuating concentration (over 20% of the time-averaged

25 concentrations). The plume ascends mildly before being purged out of the major recirculation
26 to the far field by turbulence, leading to a huge concentration difference (an order of magnitude)
27 (would it be more specific to say “leading to a huge reduction in concentration outside the near-
28 wake”?). In the far-field, the plume is higher than the tailpipe and disperses in a conventional
29 Gaussian distribution manner. Under this circumstance, a sampling duration for remote sensing
30 longer than h/U_∞ would be prone to underestimating the tailpipe emission.

31

32 *Keywords:* Dispersion models, Heavy-duty truck, Large-eddy simulation (LES), Remote
33 sensing technology, Sampling inaccuracy, Tailpipe emission.

34

35 **1. Introduction**

36 Automobile emission is a major air pollutant source, especially in mega cities where
37 vehicles and pedestrians are in close proximity (Anenberg et al. 2017). It is one of the most
38 serious threats for human health in congested urban areas (Ning et al. 2005). With a growing
39 demand for quality life and inhabitation environment, urban air quality is a major public
40 concern nowadays (Gosse et al. 2006). Source control is the most effective solution to air
41 pollution, yet reliable methods to determine the tailpipe emissions from a large number of in-
42 use vehicles are vital to enforcement (Owais 2019). Among others, remote sensing is a well-
43 established technique that has been successfully implemented for years (Cadle and Stephens
44 1994).

45

46 Remote sensing is most cost-effective in terms of coverage, deployment and manpower
47 (Xie et al. 2004). Single, instantaneous pass-by measurement in short sampling duration (less
48 than 1 sec), however, is prone to error that degrades the confidence and even ends up with false
49 detections (Huang et al. 2018). In fact, the flows around an on-road vehicle is inherently three-

50 dimensional (3D), exhibiting complicated dynamics such as separations, recirculations and
51 longitudinal vortices (Choi et al. 2014). The intermittency also imposes a technical challenge
52 for airborne pollutant measurements, which would further impair on-road remote sensing
53 (Zhang et al. 2015). Most studies have focused on the aerodynamic performance (for safety
54 and control) of vehicles but not environmental performance such as the exhaust plume
55 dispersion (Rohit et al. 2019). This study is an extension of our previous one (Huang et al. 2020)
56 in which certain good practices of remote sensing, such as valid measurement range and time,
57 were proposed. In this paper, we elaborate on the dynamics and the dispersion mechanism
58 behind. Large-eddy simulation (LES) is employed to examine in detail the unsteady flows and
59 transport after an on-road, heavy-duty truck. The outcome could help improve remote sensing
60 implementation, strengthen environmental management as well as better protect the health of
61 pedestrians and other stakeholders.

62 The wake after an on-road vehicle is broadly divided into two distinct regions, namely,
63 the near-wake and the far field (Hucho 1987). The near-wake is characterized by the intensive
64 (spanwise) recirculation immediately behind the vehicle body together with a pair of counter-
65 rotating (streamwise) trailing vortices (Vino et al. 2005). They are initiated by several factors
66 such as flow separation and wake pumping (Baker 2001) that subsequently affect the
67 aerodynamic forces and moments experienced by the vehicle (Ahmed et al. 1985). These flow
68 features play equally important roles in the transport processes for environmental concern
69 (Ahmed 1981) but have been less studied. Vehicular pollutants right after tailpipe are diluted
70 rapidly by the near-wake recirculation before detrainment (Wang et al. 2013). The far field, on
71 the other hand, consists of general turbulence behaviours without discernible flow structures
72 (Baker, 2001). Its plume dispersion is thus well predicted by the Gaussian theory, including
73 CALINE (California Line Source Dispersion Model; Benson 1992), OSPM (Operational Street
74 Pollution Model; Berkowicz 2000) and HIWAY Model (Rao and Keenan 1980). In view of the

75 persistent recirculations, the near-wake dispersion deviates from the Gaussian distribution
76 (Zhao et al. 2015). A mixing zone with uniform turbulence was used in Gaussian models to
77 handle vehicular wake effects (Zhang and Batterman 2013), which, however, often under-
78 predicted the concentrations (Kota et al. 2013). The Gaussian models also under-estimated the
79 streamwise diffusion which is important to near-field dispersion (Xing and Brimblecombe
80 2018). Moreover, the vehicle momentum suppresses dispersion but forces the pollutants
81 following its trajectory (Pospisil et al. 2004). However, these transport processes are hard to be
82 simulated in the Gaussian models. Currently, a handful of statistical models have been
83 developed for near-wake dispersion based on the Ahmed vehicle model only (Dong and Chan
84 2006). The conventional solution therefore must be interpreted cautiously to determine the
85 pollutant concentrations in the near-wake of an on-road vehicle.

86

87 Near-wake recirculation is important to the entire mixing processes after an on-road
88 vehicle because it determines the initial pollutant strength and configuration. Hence, there is a
89 need to unveil the limitations of conventional Gaussian models (Clifford et al. 1997; Gosse et
90 al. 2011). All along, Ahmed vehicle models have been commonly adopted in studies for
91 simulating real-life scenarios. In this study, a heavy-duty commercial truck, which is available
92 on the market, is used instead to include the surface details in the calculation. It has the typical,
93 square-back, in which the after-vehicle flows differ from those of a fast-back one (Hu et al.
94 2015). Massive flow separations and reattachments are observed at the trunk while a large, 3D
95 recirculation is formed downstream at the base (Choi et al. 2014). Near-wake dispersion is
96 tightly coupled with the complicated flows so additional effort is made to analyse the transport
97 processes. Likewise, the majority of far-field dispersion can be well characterized by simple
98 nondimensionalization techniques but not those in the near wake within a few vehicle heights
99 (Chang et al. 2009b).

100 In view of the inadequacy of the conventional Gaussian models for estimating near-
101 wake dispersion, wind tunnel experiments and computational fluid dynamics (CFD) have been
102 adopted to tackle the problems. Using wind tunnel measurements, Kanda et al. (2006)
103 contrasted the plume dispersion behind a passenger car with that behind a truck, focusing on
104 the relationship between velocity and pollutant concentrations. It was found that the presence
105 of the vehicle body augments the pollutant dispersion significantly. Moreover, the pollutant
106 distribution is closely related to the mean and fluctuating velocities around the vehicle. Gosse
107 et al. (2011) also employed wind tunnel measurements to study the dispersion after a simplified
108 car model, considering the possibility of chemical reactions between vehicular emissions and
109 the ambient atmospheric constituents. Although wind tunnel experiments are powerful tools
110 for dispersion studies, it hardly captures the fast, transient processes after a moving bluff body
111 in detail, such as the wake dynamics after an on-road vehicle. The one single uncontrollable or
112 unpredictable factor would further induce uncertainty (Carpentieri et al. 2012). CFD, on the
113 other hand, enables a refined spatio-temporal resolution of the flows as well as transport
114 processes. It is therefore commonly used to diagnose the fundamental physics (Cheng and Liu
115 2011). Among CFD approaches, LES is appealing for studying the transient phenomena of
116 fluid dynamics (Lesieur et al. 2018). It explicitly solves most of the conservation of momentum,
117 mass and energy while modelling small portions of Reynolds stresses and pollutant fluxes at
118 reasonable computation resources.

119

120 This section outlines the background of the problems and reviews the literature. The
121 mathematical model and boundary conditions (BCs) are recorded in the next section. Results,
122 including the flows, turbulence and dispersion, are reported in Section 3. The implication for
123 remote sensing is discussed in Section 4. The conclusion is drawn in Section 5.

124

125 **2. Methodology**

126 **2.1 Governing Equations**

127 In this paper, the LES is conducted by the open-source CFD code OpenFOAM 6
 128 (Weller et al. 1998). The flows are assumed incompressible and isothermal because buoyancy
 129 effect is limited to the proximity of tailpipes (Kanda et al., 2006). The filtered continuity

$$\frac{\partial \bar{u}_i}{\partial x_i} = 0 \quad (1)$$

130 and the filtered Navier-Stokes equation

$$\frac{\partial \bar{u}_i}{\partial t} + \frac{\partial}{\partial x_j} \bar{u}_i \bar{u}_j = -\frac{\partial \bar{\pi}}{\partial x_i} + \nu \frac{\partial^2 \bar{u}_i}{\partial x_j \partial x_j} - \frac{\partial \tau_{ij}}{\partial x_j} \quad (2)$$

131 are solved for the flows. Here, u_i is the velocity component in the i -direction, x_i the Cartesian
 132 coordinate, t the time and ν the kinematic viscosity. The summation convention on repeated
 133 indices ($i, j = 1, 2$ and 3) applies. The overbar $\bar{\psi}$ denotes the spatial filtering employed to derive
 134 the LES resolved scales. The modified resolved-scale pressure

$$\bar{\pi} = \bar{p} + \frac{2}{3} k_{SGS} \quad (3)$$

135 where p is the kinematic pressure and k_{SGS} ($= \tau_{ii}/2$) the subgrid-scale (SGS) turbulence kinetic
 136 energy (TKE). The anisotropic part of SGS momentum flux τ_{ij} ($= \overline{u_i u_j} - \bar{u}_i \bar{u}_j$) is modelled by
 137 the Smagorinsky model (Smagorinsky 1963)

$$\tau_{ij} = -2\nu_{SGS} S_{ij} + \frac{2}{3} k_{SGS} \delta_{ij} \quad (4)$$

138 where ν_{SGS} ($= C_k k_{SGS}^{1/2} \Delta$) is the SGS kinematic viscosity, S_{ij} ($= [\partial \bar{u}_i / \partial x_j + \partial \bar{u}_j / \partial x_i] / 2$) the
 139 rate-of-strain tensor, Δ ($= [\Delta_x \Delta_y \Delta_z]^{1/3}$) the filter width expressed as the cube root of the volume
 140 of hexahedral cell, δ_{ij} the Kronecker delta and C_k ($= 0.07$) a modelling constant. The SGS TKE
 141 conservation is handled by the one-equation TKE model (Schumann 1975)

$$\frac{\partial k_{SGS}}{\partial t} + \frac{\partial}{\partial x_i} k_{SGS} \bar{u}_i = 2\nu_{SGS} S_{ij} S_{ij} + (\nu + \nu_{SGS}) \frac{\partial^2 k_{SGS}}{\partial x_i \partial x_i} - C_\epsilon \frac{k_{SGS}^{3/2}}{\Delta} \quad (5)$$

142 where $C_\epsilon (= 1.05)$ is another modelling constant. The filtered pollutant transport equation

$$\frac{\partial \bar{\phi}}{\partial t} + \frac{\partial}{\partial x_i} \bar{\phi} \bar{u}_i = \frac{\nu + \nu_{SGS}}{Sc} \frac{\partial^2 \bar{\phi}}{\partial x_i \partial x_i} \quad (6)$$

143 is solved for the dispersion where ϕ is the pollutant concentration and $Sc (= 0.72)$ the Schmidt
144 number.

145

146 2.2 Computational Domain and Boundary Conditions

147 The model of the heavy-duty truck (Figure 1a) sizes $3.86h$ (length) \times $0.89h$ (width) \times
148 $1.09h$ (height) while the computational domain is (Figure 1b) $31.8h$ (streamwise) \times $3.9h$
149 (spanwise) \times $10.3h$ (vertical). Here, h is the height of the truck (Can we give the value of h so

150 that readers will know if it is a real-size or small-scale model? Also readers may want to know
151 the value of wind speed and the pollutant source (e.g. the pollutant species (CO_2 , CO , NO_x ?),
152 the exhaust flow rate, pollutant concentrations at tailpipe exit). Dirichlet BCs (boundary
153 conditions? Please define abbreviations before use) of constant wind speed U_∞ and zero

154 pollutant $\bar{\phi} = 0$ are prescribed at the inflow. The prevailing flows are thus in the streamwise x
155 direction normal to the wind shield of the truck. The logarithmic law of the wall (log-law) is
156 used to model the flow BCs on all the solid boundaries including the ground and the truck body.

157 At the domain top and the spanwise extent, Neumann BCs ($\partial \bar{\psi} / \partial \bar{n} = 0$ where \bar{n} is the normal
158 to the boundary surface) for both flows and dispersion are applied. A pollutant (point) source
159 of size $20 \times 10^{-6} h^3$ with a constant emission rate \dot{Q} is placed at the tailpipe exhaust ($x = 0, y =$
160 $0, z = 0$) to simulate vehicular pollutant. The effect of exhaust-induced turbulence is limited

161 and (?) close to the tailpipe so the emission speed is not considered (Chan et al. 2001). An open

162 BC ($\partial \bar{\phi} / \partial t + \bar{u} \partial \bar{\phi} / \partial x = 0$) is applied at the outflow so all the pollutants are removed from the

163 computational domain by the prevailing flows without any reflection. Neumann BCs for
 164 pollutants are adopted on all the solid boundaries. The Reynolds number based on the free-
 165 stream wind speeds U_∞ (characteristics velocity scale) and the trunk height h (characteristic
 166 length scale) $Re (= U_\infty h/\nu)$ is over 37,200 that is comparable to that in previous studies (Tunay
 167 et al. 2016). The characteristic pollutant concentration $\Phi_0 = \dot{Q}/U_\infty h^2$ is approximately the far-
 168 field value.

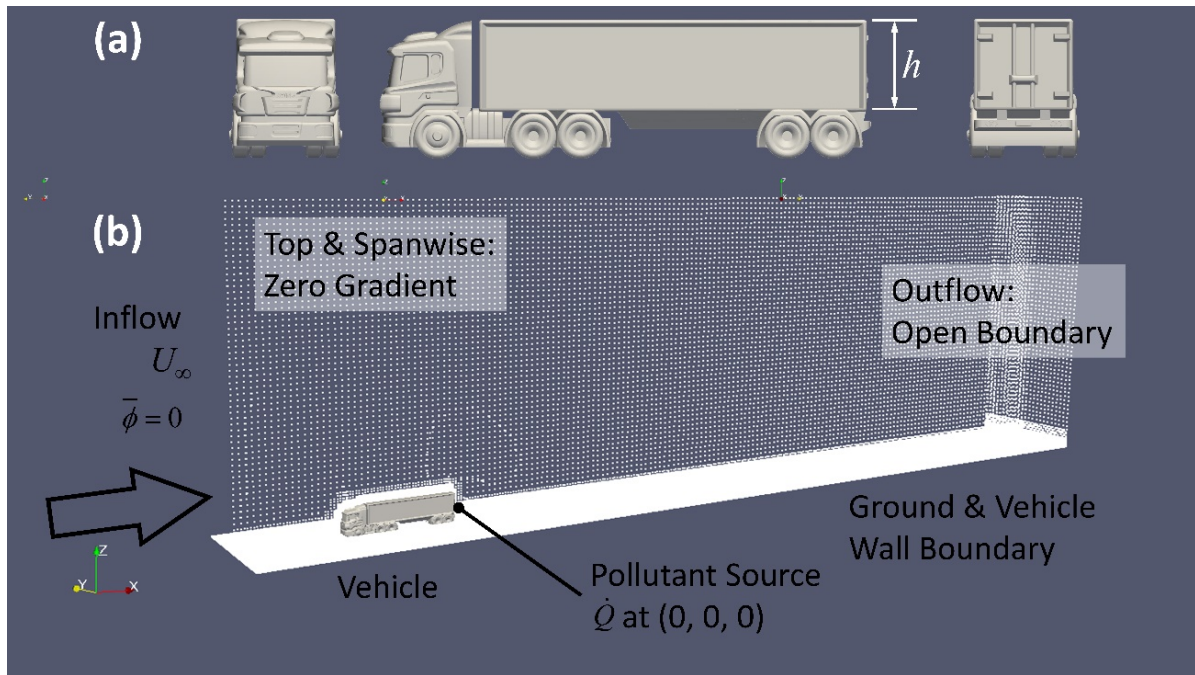


Figure 1. (a) The digital model of the heavy-duty truck together with (b) computational domain and boundary conditions.

169

170 2.3 Numerical Method

171 The spatial domain is discretized into 3.38 million unstructured hexahedra. The cells are refined
 172 towards the truck surfaces and the ground by the mesh generation utility *snappyHexMesh*
 173 (OpenFOAM 2018). The minimum and maximum cell volume is in the order of $10^{-7}h^3$ and 10^{-}
 174 $^2h^3$, respectively. The size of the cells is thus ranged from $0.005h$ to $0.2h$. The time-step
 175 increment is $\Delta t = 0.0013h/U_\infty$. The finite volume method (FVM) is used to solve the

176 mathematical model. The implicit, second-order-accurate backward differencing is employed
177 in the time integration. The gradient, divergence and Laplacian terms are integrated by the
178 second-order-accurate Gaussian FVM based on the summation on cell faces. The pressure-
179 implicit with splitting of operators (PISO) approach is used to handle the pressure-velocity
180 coupling in incompressible flows. The preconditioned conjugate gradient (PCG) method is
181 used to solve the symmetric equation system of pressure and the preconditioned bi-conjugate
182 gradient (PBiCG) method is used to solve the asymmetric systems of other variables. The
183 residual of the iterative solvers is less than 10^{-8} for converged solution. Equations are integrated
184 in time for $30h/U_\infty$ to initialize the flows and dispersion. After pseudo-steady state, they are
185 integrated for another $30h/U_\infty$ to compute the statistics. The data sampling time is long enough
186 to ensure convergence of first- and second-order moments. In the following analyses, the angle
187 brackets $\langle \psi \rangle$ denote time average (mean) while the double prime ψ'' ($= \psi - \langle \psi \rangle$) denotes the
188 deviation from the time average $\langle \psi \rangle$.

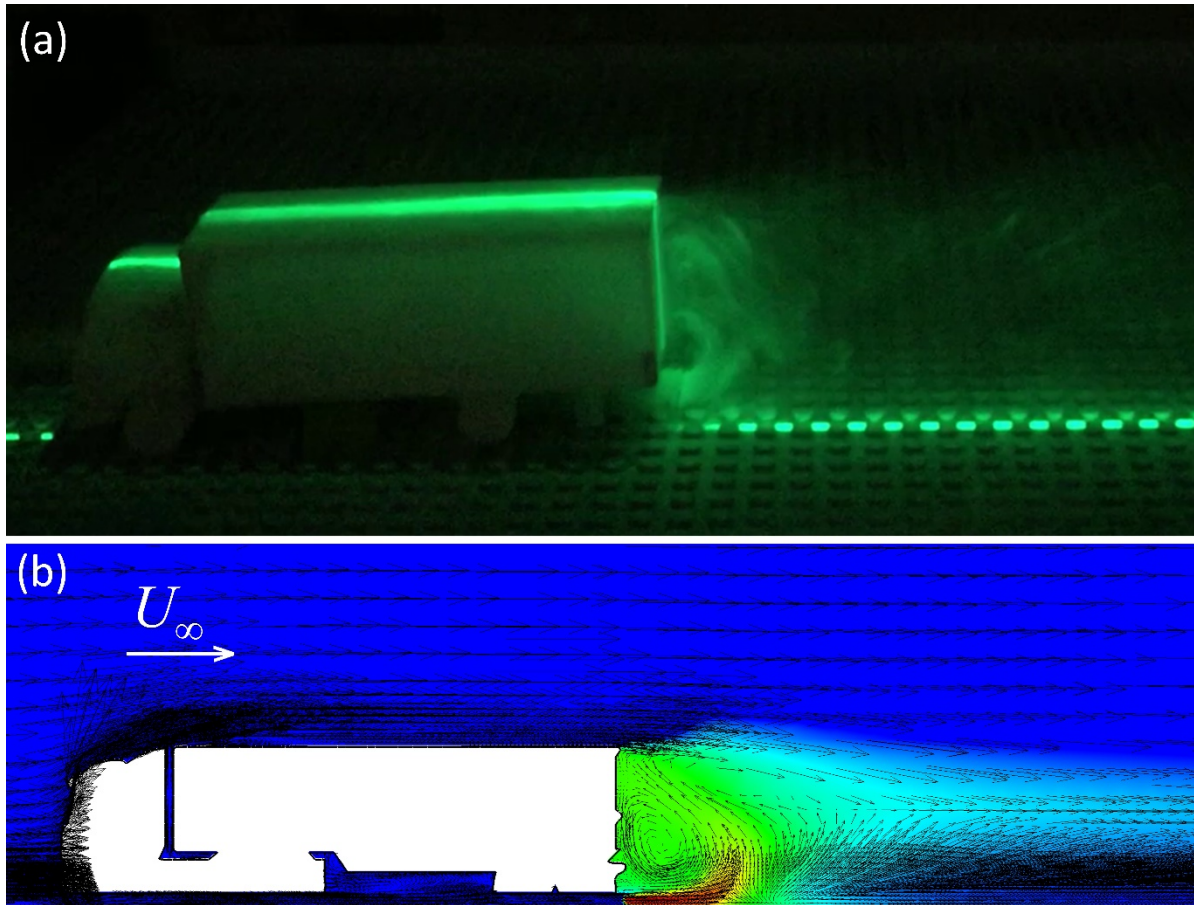


Figure 2. Visualization of the near-wake flows after a heavy-duty truck in: (a). previous wind tunnel experiment (Liu et al. 2019) and (b). the current LES.

189 3. Results

190 3.1 Flows

191 Both our previous wind tunnel visualization (Liu et al. 2019) and the current LES
 192 illustrate that the near wake after a truck consists of a major recirculation of size h (Figure 2).
 193 The recirculation (reverse flow) is highly 3D and emanates from the truck underbody toward
 194 the rear side. A similar flow pattern was reported schematically in laboratory experiments
 195 (Chang et al. 2009a). It is thus expected that the pollutant concentration is more homogeneous
 196 within the major recirculation. In this connection, a box model was proposed to determine the
 197 pollutant concentrations in the immediate vicinity of a roadway (Habegger et al. 1974) instead
 198 of the conventional Gaussian model. Over the trunk, another counter-rotating, upper
 199 recirculation is developed, which is in line with the existing LESs (Chan et al. 2008; Minguez

200 et al. 2008) as well as laboratory experiments (Wang et al. 2013; Sellappan et al. 2018). These
 201 recirculations are sensitive to vehicle shape, such as the rear slant angle, which tremendously
 202 affects the near-wake structure. We thus disentangle the pollutant transport mechanism from
 203 the dynamics to explore the technical difficulty of remote sensing.

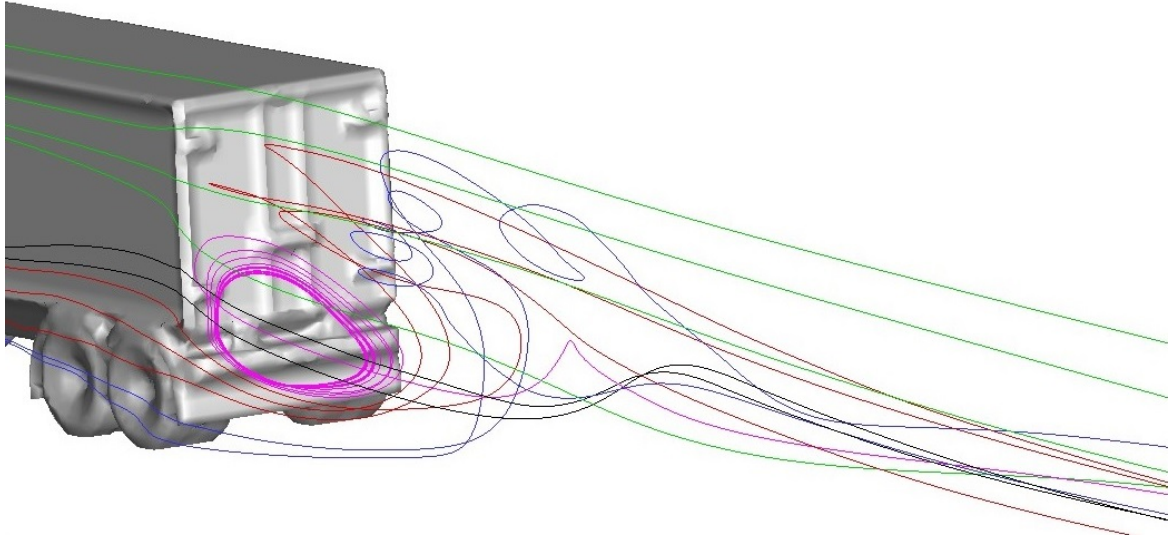


Figure 3. Streamlines illustrate the flows entrainment from the side into the near wake after the truck.

204 Although the upper recirculation is merely visualized in the wind tunnel experiment,
 205 the tracer being emitted from the tailpipe is elevated to the upper part of the truck after the near
 206 wake (Figure 2a), which is in line with the current LES (Figure 2b). The flows entraining from
 207 the side are divided into three parts (Figure 3). The bottom part, which essentially climbs up a
 208 height of h , forms the outer region surrounding the major recirculation as well as initiates the
 209 upper recirculation. The top part is mainly driven by the prevailing flows that does not show
 210 noticeable meandering. The middle part immerses into the major recirculation. These structures
 211 align with those reported in the literature (McArthur et al. 2016).

212

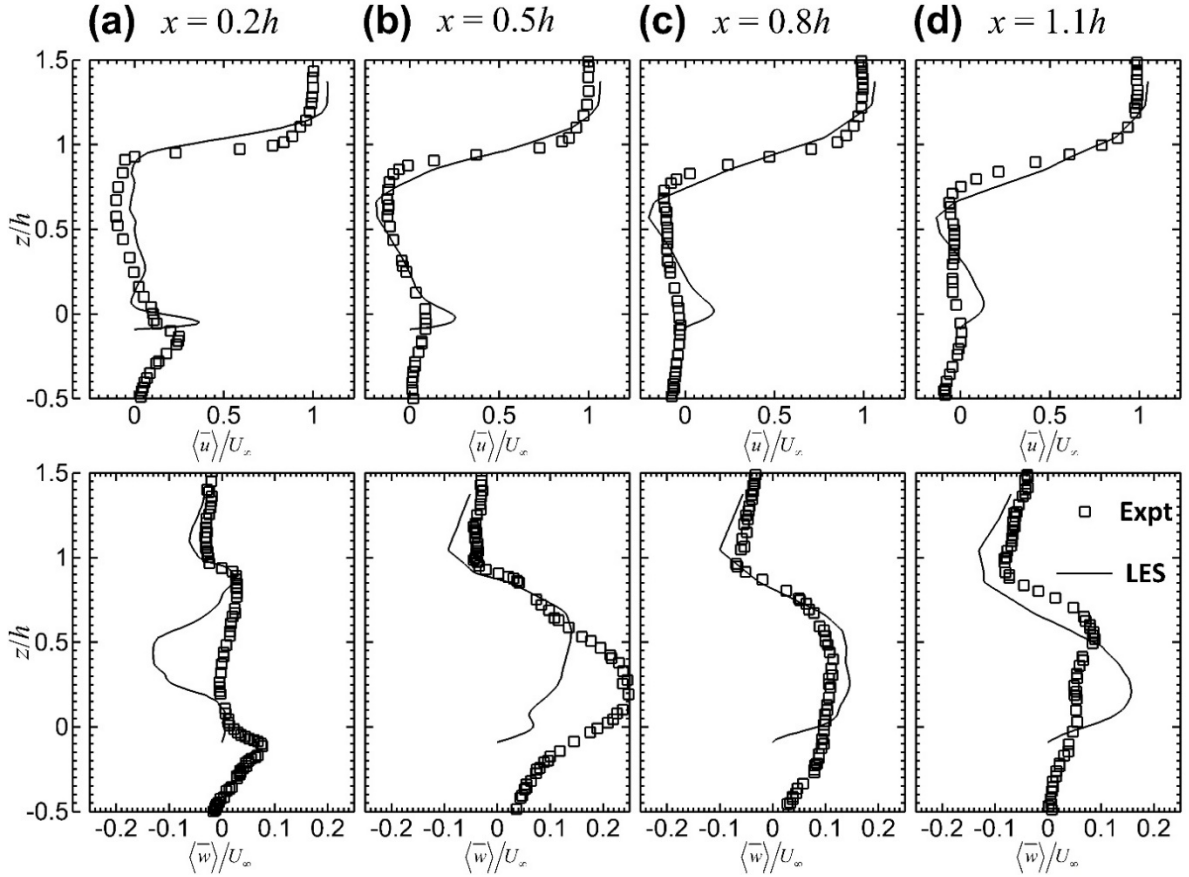


Figure 4. Vertical dimensionless profiles of mean streamwise $\langle \bar{u} \rangle / U_\infty$ and vertical $\langle \bar{w} \rangle / U_\infty$ velocities on the vertical (x - z) centre plane at $y = 0$ for $x/h =$ (a). 0.2, (b). 0.5, (c). 0.8 and (d). 1.1. The experimental data are obtained from Lo and Kontis (2017).

213 Apart from the visualization, the current LES is validated by the wind tunnel results
 214 available in the literature (Lo and Kontis 2017). The near-wake velocity profiles obtained from
 215 the two solutions, especially the roof-level mixing layer, compare well with each other (Figure
 216 4). The LES-calculated wall jet is slightly stronger than that of the wind tunnel. Discrepancy
 217 in the vertical flows is observed in the core of major recirculation. It could be attributed to the
 218 dissimilar vortex centres in the two studies. A strong wind shear (velocity difference $\Delta \langle \bar{u} \rangle \approx$
 219 U_∞) and a mild wall jet ($0.1U_\infty \leq \Delta \langle \bar{u} \rangle \leq 0.3U_\infty$) are developed, respectively, about the roof
 220 level ($z \approx h$) and below the trunk ($z \leq 0$). The upper flows are induced by the prevailing wind

221 and pressure difference while the bottom wall jet is driven by the flows from the truck
 222 underbody. Moreover, mild downward ($-0.1U_\infty \leq \langle \bar{w} \rangle$) and upward ($\langle \bar{w} \rangle \leq 0.25U_\infty$) flows are
 223 observed at the top and bottom, respectively. These flow structures constitute the major
 224 recirculation, governing the rapid, early plume mixing. Close to the trunk at $x = 0.2h$, the
 225 underbody wall jet is noticeable ($\langle \bar{u} \rangle = 0.3U_\infty$ and $\langle \bar{w} \rangle = 0.1U_\infty$; Figure 4a) that picks up the
 226 tailpipe emission. The flows then bend upwards ($\langle \bar{u} \rangle \leq 0.1U_\infty$ and $0.1U_\infty \leq \langle \bar{w} \rangle \leq 0.2U_\infty$) at
 227 $x = 0.5h$ (Figure 4b) and continue at $x = 0.8h$ (Figure 4c). The peaked vertical flows are further
 228 elevated to $z = 0.2h$ at $x = 1.1h$ (Figure 4d) close to the boundary of the major recirculation.

229

230 The truck models employed in the wind tunnel experiments and the current LES possess
 231 a few minor differences, such as the accessories on the bodies and the size of the truck, leading
 232 to the discrepancy in the wake structures observed. Nonetheless, they have the common fast-
 233 back design so the near-wake flow structures are representative and generally agree with each
 234 other.

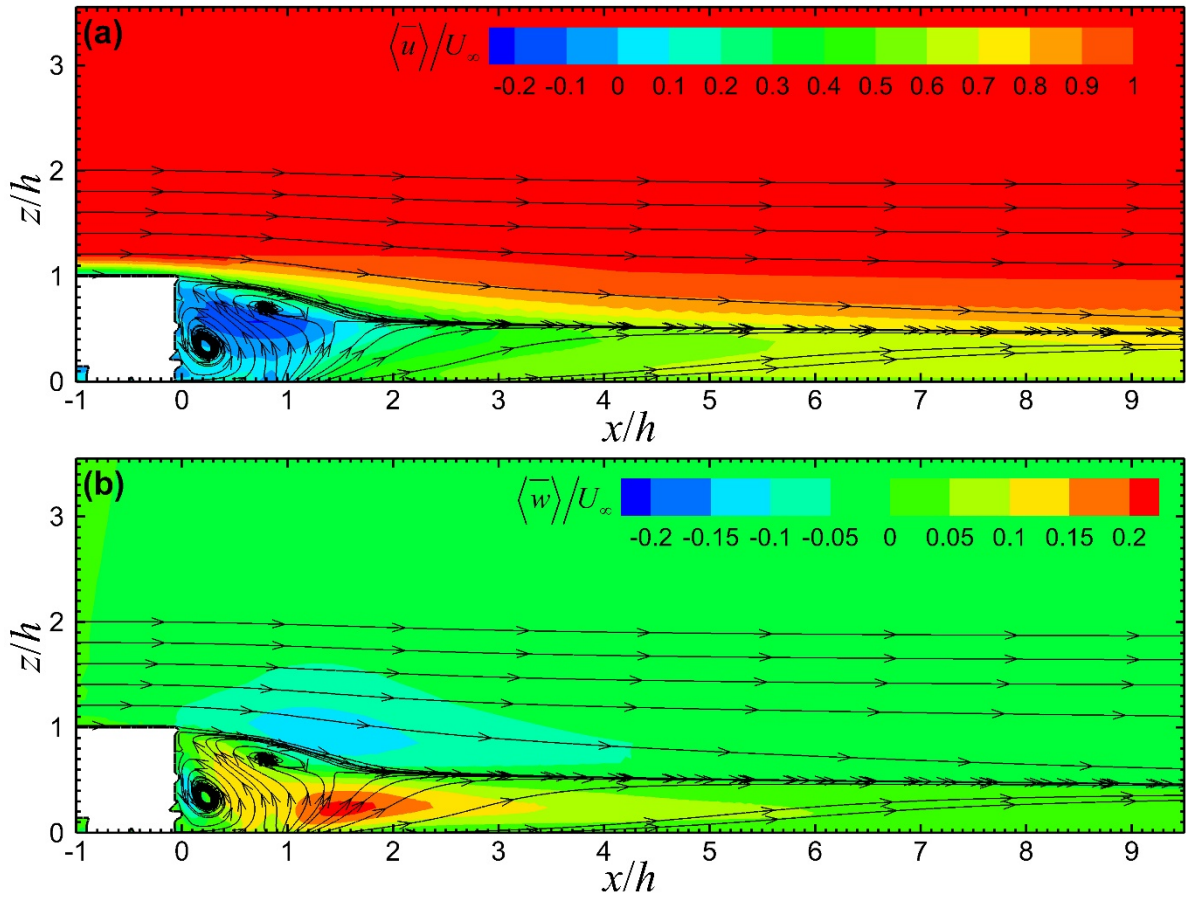


Figure 5. Shaded contours of dimensionless (a). streamwise $\langle \bar{u} \rangle / U_\infty$ and (b). vertical $\langle \bar{w} \rangle / U_\infty$ mean velocities on the vertical (x - z) centre plane at $y = 0$. Also shown are the streamlines.

235

236

237

238

239

240

241

The major and upper recirculations in the near wake ($x \leq h$) are depicted by the LES-calculated streamlines and velocities (Figure 5). Substantial reverse flows ($\langle \bar{u} \rangle \leq 0$) are observed in the near wake whose extremity ($\langle \bar{u} \rangle = -0.25U_\infty$) locates between the two counter-rotating recirculations ($x = 0.5h, z = 0.5h$). On top of the side entrainment, the prevailing flows descend mildly after the near wake ($x \geq h$), inducing the flow convergence at $z = 0.5h$ (Figure 5a). The convergence also serves as a group of dividing streamlines that partitions the vertical

242 flows into the upward ($\langle \bar{w} \rangle > 0$) and downward ($\langle \bar{w} \rangle < 0$) regimes (Figure 5b). The roof-level
 243 downward flows ($0 \leq x \leq 3h$) locate over the upper recirculation, transferring momentum into
 244 the near wake. The upward flows are found below the dividing streamlines, rolling from the
 245 sides towards the trunk behind the major circulation while moving downstream. They are
 246 indeed largely induced by the low-level entrainment from the side (Figure 3).
 247

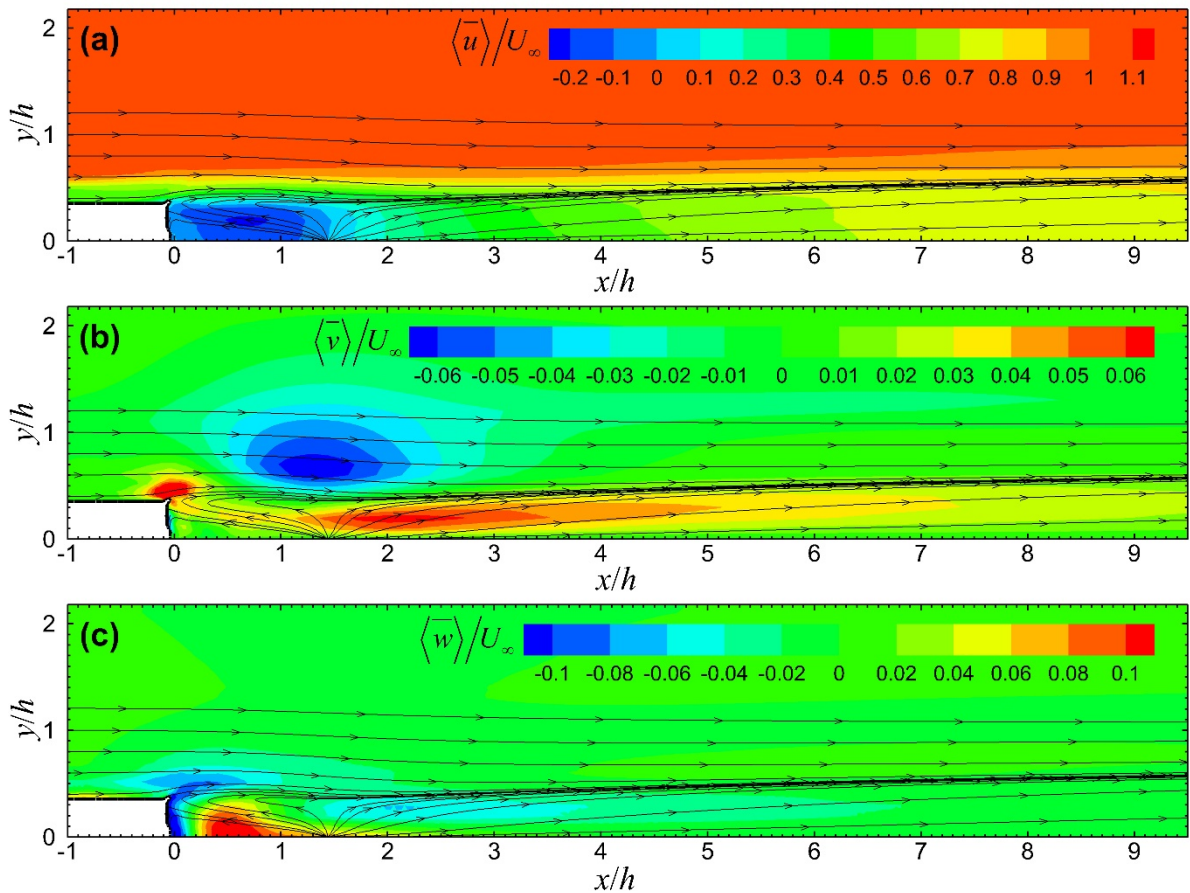


Figure 6. Shaded contours of dimensionless (a). streamwise $\langle \bar{u} \rangle / U_\infty$, (b). spanwise $\langle \bar{v} \rangle / U_\infty$

and (c). vertical $\langle \bar{w} \rangle / U_\infty$ mean velocities on the horizontal $(x-y)$ plane at $z = 0.5h$.

Also shown are the streamlines.

248

249 Flow convergence is also observed on the horizontal (x - y) plane at $z = 0.5h$, further
 250 characterizing the wake flows after the truck (Figure 6). The reverse flows ($\langle \bar{u} \rangle = -0.2U_\infty$) in
 251 the major recirculation are rather uniform (Figure 6a). Similar to the vertical flows on the x - z
 252 plane, the spanwise flows are partitioned into positive and negative on the horizontal (x - y)
 253 plane (Figure 6b). Apart from the flow separation at the truck edge before the wake, a mild,
 254 positive (outward) flow regime ($\langle \bar{v} \rangle = 0.06U_\infty$) is elongated ($1.5 \leq x/h \leq 3.5$) after the major
 255 recirculation, developing the flow convergence on the sides. On the other hand, negative
 256 spanwise flows ($\langle \bar{v} \rangle = -0.06U_\infty$) are found between the near wake and the far field ($x = 1.5h$).
 257 They reside outside the convergence ($y \geq 0.4h$), which signifies the flow entrainment from the
 258 sides, though with weaker intensity (by 3 times) than the case of the vertical flows on the
 259 vertical centre plane (Figure 5). Both the time-averaged spanwise and vertical flows are
 260 towards the core at the same streamwise location ($0 \leq x \leq 3h$) that collectively enforce the flow
 261 convergence. Downward flows ($\langle \bar{w} \rangle = -0.1U_\infty$) are found after the truck edge on the horizontal
 262 plane (Figure 6c) that concur the three characteristic regimes discussed in Figure 3. After the
 263 major recirculation ($x \geq h$), the flows descend slightly ($\langle \bar{w} \rangle = -0.05U_\infty$), diminishing gradually
 264 in the streamwise direction.

265

266 3.2 Fluctuating Velocity

267 Turbulence $\langle u_i' u_i' \rangle^{1/2}$ after the truck is quite isotropic except close to the ground
 268 surface near the boundary of major recirculation (Figure 7). The isotropy inside the major
 269 circulation is attributed to the recirculating flows that augments the homogeneous transport.
 270 They are rather small $\langle u_i' u_i' \rangle^{1/2} \leq 0.04U_\infty$ for $x \leq 0.5h$ in the major recirculation. The
 271 streamwise ($\langle u' u' \rangle^{1/2} = 0.14U_\infty$; Figure 7a) and spanwise ($\langle v' v' \rangle^{1/2} = 0.16U_\infty$; Figure 7b)

272 fluctuating velocities elevate close to the ground surface in $h \leq x \leq 2h$. These two peaks coincide
 273 with the boundary of major recirculation where the side entrainment drives the majority flow
 274 upward. Moreover, the underbody wall jet decelerates and bends upward. The local wind shear
 275 subsequently escalates the turbulence intensity.

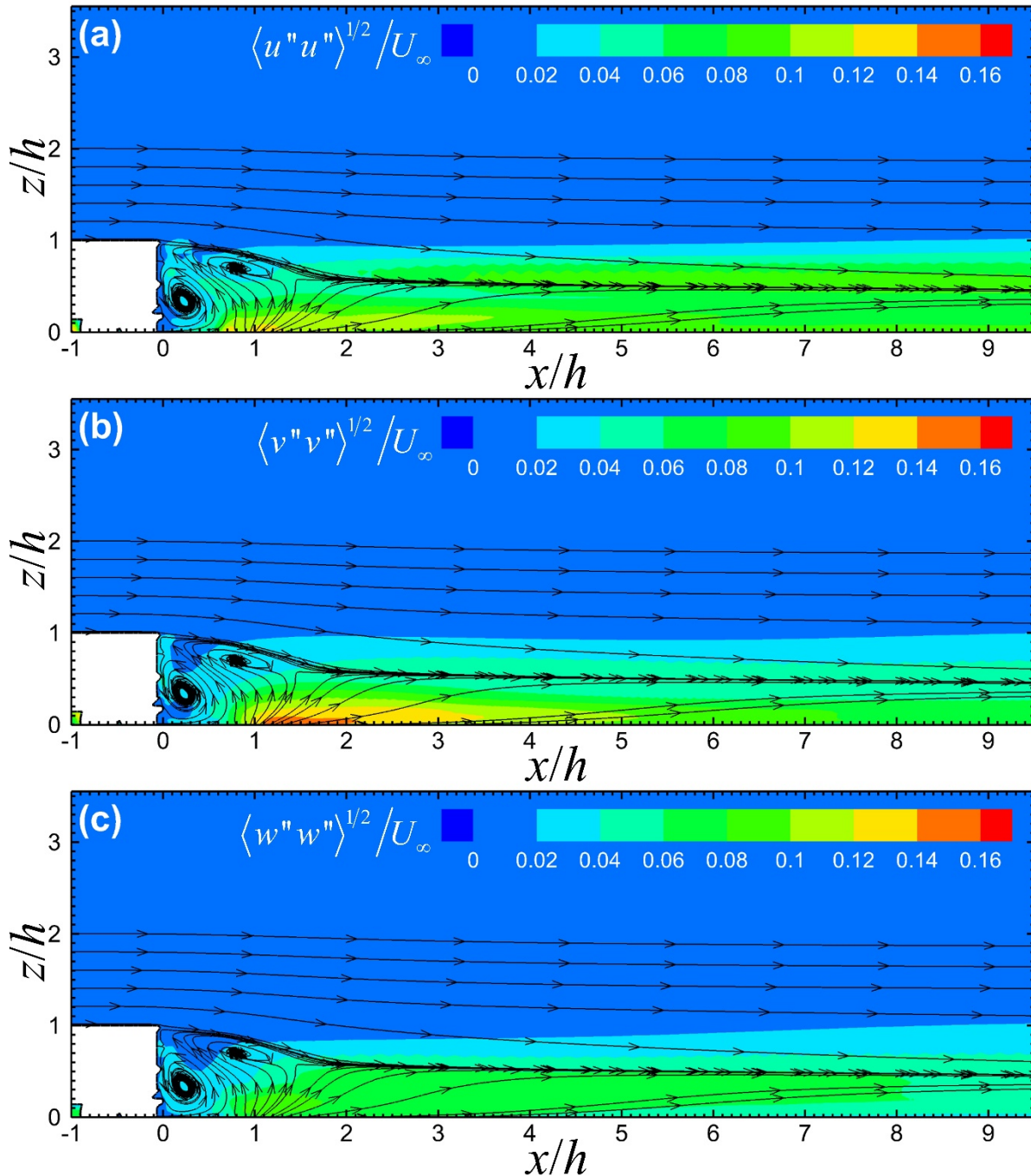


Figure 7. Shaded contours of dimensionless (a). streamwise $\langle u''u'' \rangle^{1/2}/U_\infty$, (b). spanwise $\langle v''v'' \rangle^{1/2}/U_\infty$ and (c). vertical $\langle w''w'' \rangle^{1/2}/U_\infty$ fluctuating velocities on the vertical (x - z) centre plane at $y = 0$. Also shown are the streamlines.

276

277

278

279

280

281

282

283

284

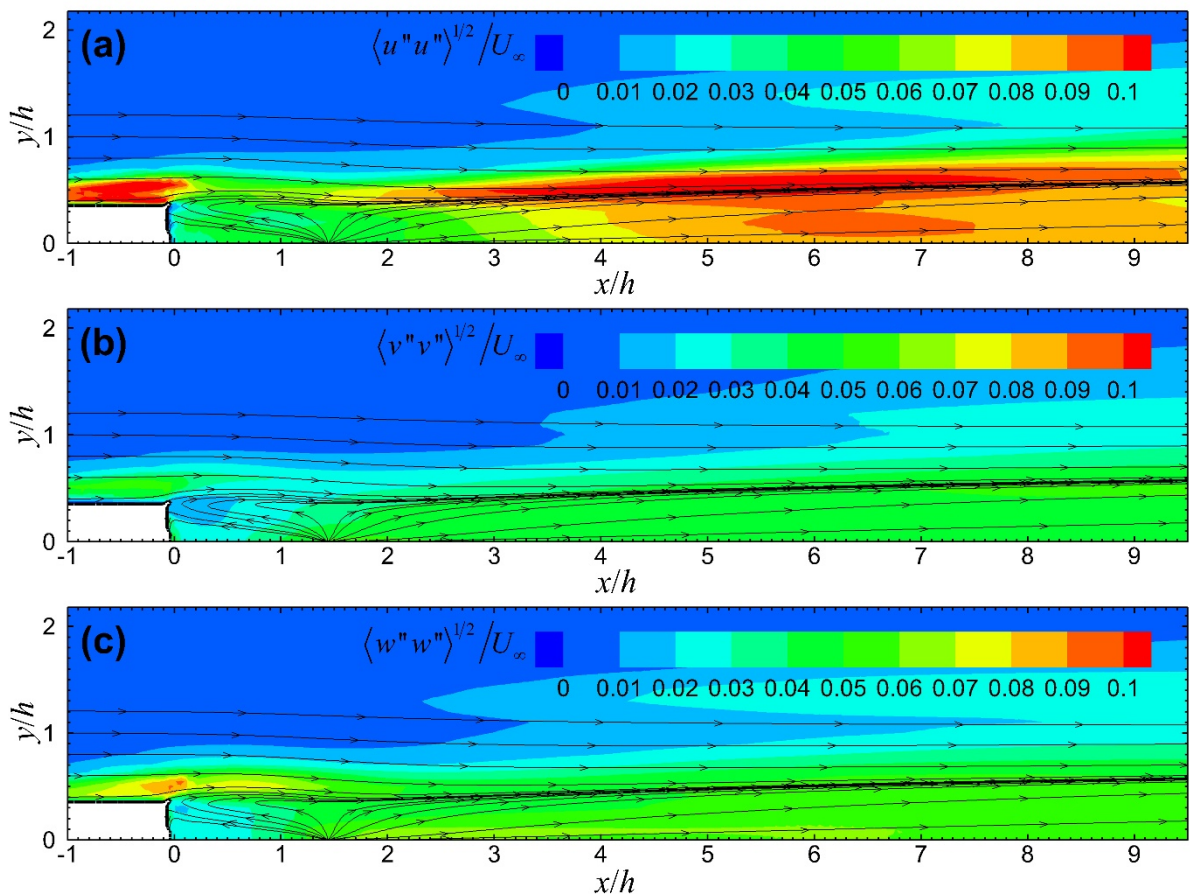


Figure 8. Shaded contours of dimensionless (a). streamwise $\langle u'u' \rangle^{1/2}/U_\infty$, (b). spanwise $\langle v'v' \rangle^{1/2}/U_\infty$ and (c). vertical $\langle w'w' \rangle^{1/2}/U_\infty$ fluctuating velocities on the horizontal $(x-y)$ plane at $z = 0.5h$. Also shown are the streamlines.

285

286

287

288

289

290

291

292

293

294

295

296

297

298

299

300 3.3. Pollutant Dispersion

301

302

303

304

305

306

The flows and turbulence discussed above form the basis to explain the plume characteristics on the vertical $(x-z)$ centre plane at $y = 0$ (Figure 9). After being emitted from the tailpipe, the pollutant is driven by the major recirculation toward the truck (Figure 9a). The reverse flows are mainly driven by the side entrainment so the pollutant is mixed rapidly within the major recirculation. Pollutant overshoot ($z \geq h$) is found in response to the upper recirculation and the elevated turbulence in the upper shear layer. The pollutant over the dividing streamlines

307 is then diluted quickly by the prevailing flows at free-stream wind speed. Concurrently, the
 308 pollutant below the flow convergence is dispersed from the major recirculation to the upper
 309 recirculation at $x = 0.8h$, $z = 0.8h$ across the streamlines. Subsequently, it is carried downstream
 310 to the far field at a level ($z = h/2$ for $x \geq h$) higher than that of the tailpipe, resulting in the
 311 elevated plume trajectory. A sharp decrease in the pollutant concentration is thereafter observed
 312 between the major recirculation and the far field.

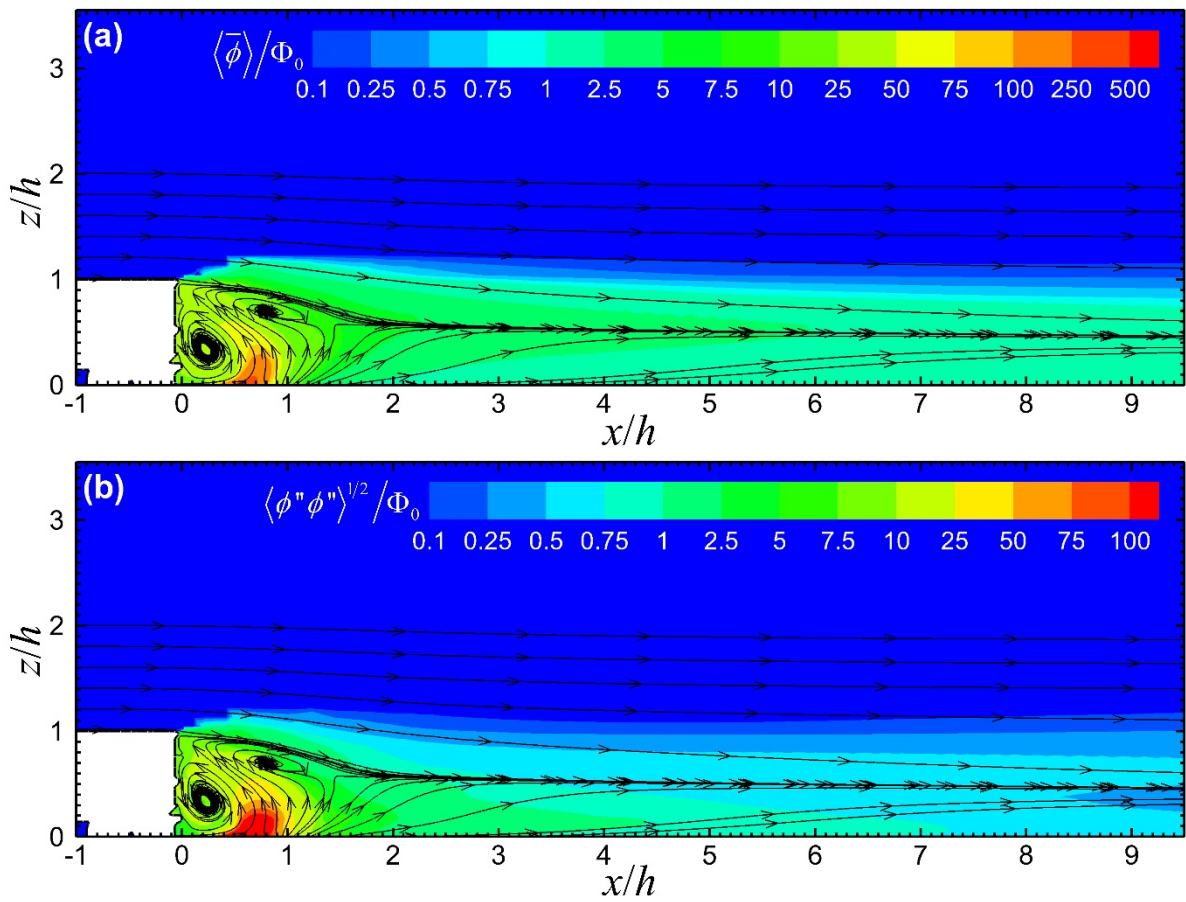


Figure. 9. Shaded contours of dimensionless (a). mean pollutant concentration $\langle \bar{\phi} \rangle / \Phi_0$ and
 (b). fluctuating pollutant concentration $\langle \phi'' \phi'' \rangle^{1/2} / \Phi_0$ on the vertical (x - z) centre
 plane at $y = 0$. Also shown are the streamlines.

313

314 The maximum fluctuating pollutant concentration ($\langle \phi'' \phi'' \rangle^{1/2} = 100\Phi_0$) is almost up to

315 20% of the mean pollutant concentration ($\langle \bar{\phi} \rangle = 250\Phi_0$) within the major recirculation that

316 decreases along the plume trajectory (Figure 9b). It is caused by the reducing mean pollutant
 317 concentrations and the enhanced mixing in the major recirculation. The fluctuating pollutant
 318 concentration decreases to $\langle \phi'' \phi'' \rangle^{1/2} \leq \Phi_0$ over the dividing streamlines. The prevailing flows
 319 dilute pollutants quickly, which in turn reduces the pollutant concentration fluctuation (is the
 320 correction OK?). Below the dividing streamlines, on the other hand, it (the pollutant
 321 fluctuation?) decreases gradually in the far field.

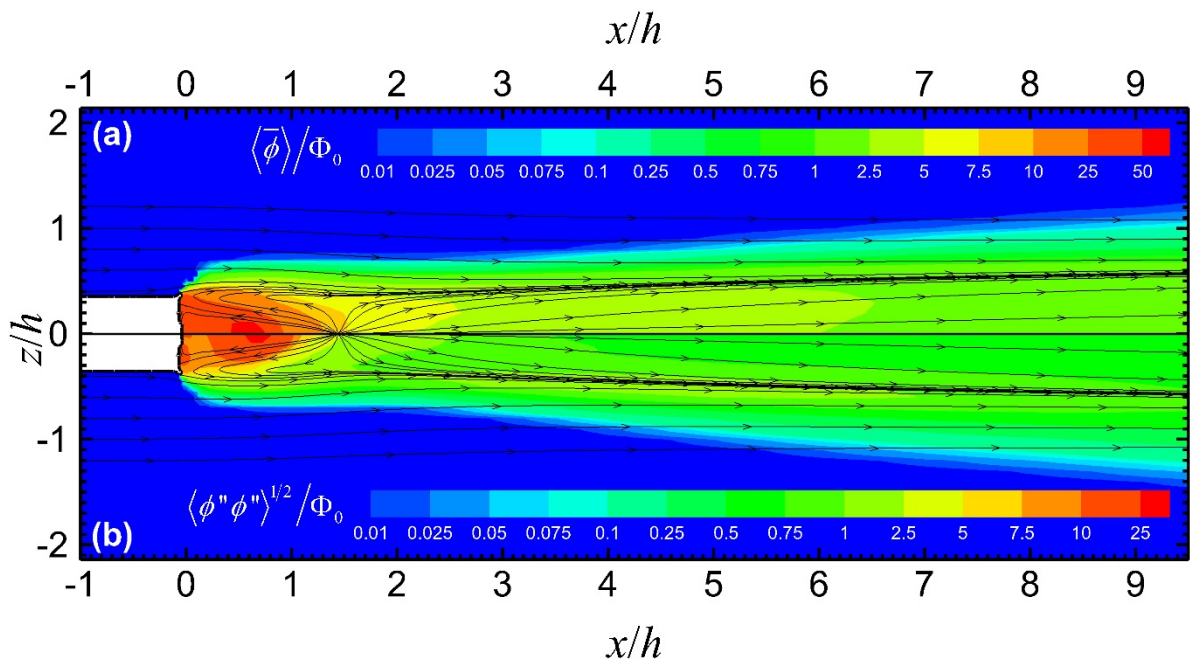


Figure 10. Shaded contours of dimensionless (a). mean pollutant concentration $\langle \bar{\phi} \rangle / \Phi_0$ and
 (b). fluctuating pollutant concentration $\langle \phi'' \phi'' \rangle^{1/2} / \Phi_0$ on the horizontal (x - y) plane at
 $z = h/2$. Also shown are the streamlines.

322

323 Recurring on the horizontal (x - y) plane at $z = h/2$, most pollutants are trapped by the
 324 major recirculation after tailpipe emission (Figure 10). The homogeneous pollutant
 325 concentration within the major recirculation is clearly observed. The mean pollutant
 326 concentration in the major recirculation ($\langle \bar{\phi} \rangle \geq 50\Phi_0$) is higher than that in the far field ($\langle \bar{\phi} \rangle$
 327 $\approx \Phi_0$) by an order of magnitude. The major recirculation thus retains a large amount of tailpipe

328 emission in a rather well-mixed manner. The dividing streamlines work together like a shelter,
 329 suppressing the pollutant removal from the major recirculation to the far field. Cross-streamline
 330 pollutant transport is governed by turbulence only that is much weaker than advection. A huge
 331 pollutant concentration gradient is thus developed between the major recirculation and the far
 332 field. thereafter. In the far field, the local maximum of mean pollutant concentration shifts from
 333 the centre at $y = 0$ sideward to $y = 0.3h$, which deviates from the Gaussian theory. (Any
 334 explanation for the shift in local max mean pollutant concentration?)

335

336 The fluctuating pollutant concentration ($\langle \phi''\phi'' \rangle^{1/2} \geq 25\Phi_0$) is elevated within the
 337 major recirculation (Figure 10b). It is as high as 50% of the time-averaged pollutant
 338 concentration ($\langle \bar{\phi} \rangle \approx 50\Phi_0$). Under this circumstance, likely the signal collected within the
 339 major recirculation, though strong, would be very noisy. In the far field, the peaked fluctuating
 340 pollutant concentration correlates tightly with the peaked mean pollutant concentration. It
 341 locates at $y = 0.5h$, displacing mildly from the peak of the mean pollutant concentration. The
 342 discrepancy could be explained by the dissimilar profiles. It is because the fluctuating pollutant
 343 concentration is proportional to the gradient of the mean pollutant concentration.

344

345 When the y - z planes are located within the major recirculation (Figures 11a to 11c), the
 346 flows are characterized by two counter-rotating vortices. They are initiated by the near-wake,
 347 low-pressure zone which entrains the flows into the major recirculation. These pair of
 348 streamwise vortices were reported elsewhere (Lo and Kontis 2017). However, on the planes
 349 outside the major recirculation (Figures 11d to 11f), the key feature is the two counter-rotating
 350 trailing vortices on the y - z plane. It is also found that the upper shear layer gradually develops
 351 that interacts with the recirculations and the trailing vortices (modifies their flow directions and
 352 sizes). The two trailing vortices persist after $x \geq 1.75h$ that drive the flows further downstream.

353 Apart from the trailing vortices, some small vortices are found near the ground which could be
 354 generated by ground-level shear.

355

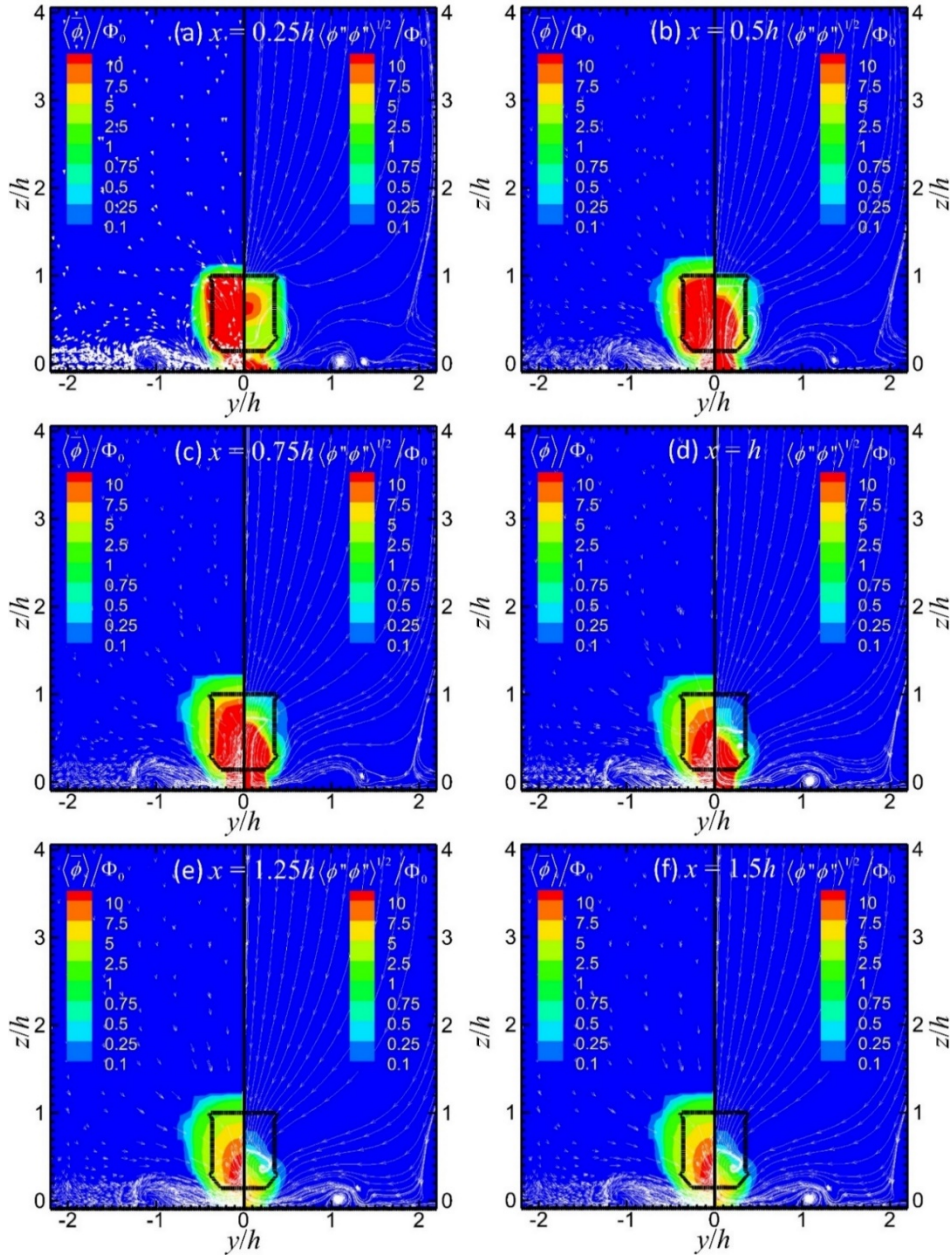


Figure 11. Shaded contours of dimensionless mean pollutant concentration $\langle \bar{\phi} \rangle / \Phi_0$ and fluctuating pollutant concentration $\langle \phi'' \phi'' \rangle^{1/2} / \Phi_0$ on the vertical (y - z) plane at $x/h =$ (a). 0.25, (b). 0.5, (c). 0.75, (d). 1, (e). 1.25 and (f). 1.5. Also shown are the flow vectors and the streamlines.

356
 357
 358
 359
 360
 361
 362
 363
 364
 365
 366
 367
 368
 369
 370
 371
 372
 373

The tailpipe is located close to the plane at $x = 0.25h$ (Figure 11a) so there is a small region with elevated mean and fluctuating pollutant concentrations. The fluctuating pollutant concentration at $z = 0.7h$ is further intensified by the shear between the major and upper recirculations. The pollutant removal from the major recirculation is thus enhanced. The major recirculation mixes the pollutant rapidly (Figures 11b and 11c). The underbody wall jet drives the pollutant upwards so the mean pollutant concentration is rather uniform behind the truck (Figure 11b). The peaked time-averaged pollutant concentration then descends slightly after the major recirculation (Figure 11c). The coverage of fluctuating pollutant concentration at $x = 0.5h$ (Figure 11b) and $x = 0.75h$ (Figure 11c) is similar. It reflects the turbulent pollutant transport from the recirculations into the trailing vortices. In the far field ($x \geq h$), the pollutant is diluted quickly by the prevailing flows that is represented by the fast decreasing mean and fluctuating concentrations (Figure 11d and 11f). The slight descent of the upper shear layer is also observed (Figures 11d to 11e) that eventually converges for $x \geq 1.25h$ (Figures 11e and 11f). The peaked mean pollutant concentration remains at $z = 0.5h$. On the other hand, the peaked fluctuating concentration further descends (Figures 11e and 11f), resulting in a ground-level maximum.

374
 375

3.4 Transport Mechanism

376
 377
 378
 379
 380

The streamwise mean pollutant flux on the vertical (x - z) centre plane at $y = 0$ shows elongated ($0 \leq x \leq 4h$), positive streamwise mean pollutant flux ($\langle \bar{\phi} \rangle \langle \bar{u} \rangle = 2\Phi_0 U_\infty$) over the dividing streamlines (Figure 12a). It in turn illustrates the mild advection of the pollutant overshoot by the strong prevailing flows. In the major recirculation, the abandon tailpipe emission close to the unbody wall jet results in the maximum streamwise mean pollutant flux

381 $\langle \overline{\phi} \rangle \langle \overline{u} \rangle = 10\Phi_0 U_\infty$) near the ground at $x = h/2$. The flows reverse afterwards, leading to the
 382 minimum streamwise mean pollutant flux ($\langle \overline{\phi} \rangle \langle \overline{u} \rangle = -10\Phi_0 U_\infty$) at $z = h/2$. These two equal-
 383 magnitude streamwise mean pollutant fluxes in opposite directions together with the local
 384 maximum vertical mean pollutant flux ($\langle \overline{\phi} \rangle \langle \overline{w} \rangle = 10\Phi_0 U_\infty$) at the ground level (Figure 12b)
 385 develop the pollutant recirculation and the thorough mixing. Hence, the vehicular emission is
 386 escalated from the tailpipe to the upper recirculation, resulting in the rather uniform
 387 concentration within the major recirculation (Figures 9 and 10). The mean pollutant fluxes
 388 decrease gradually in the far field because of the diminishing vertical mean flow.
 389

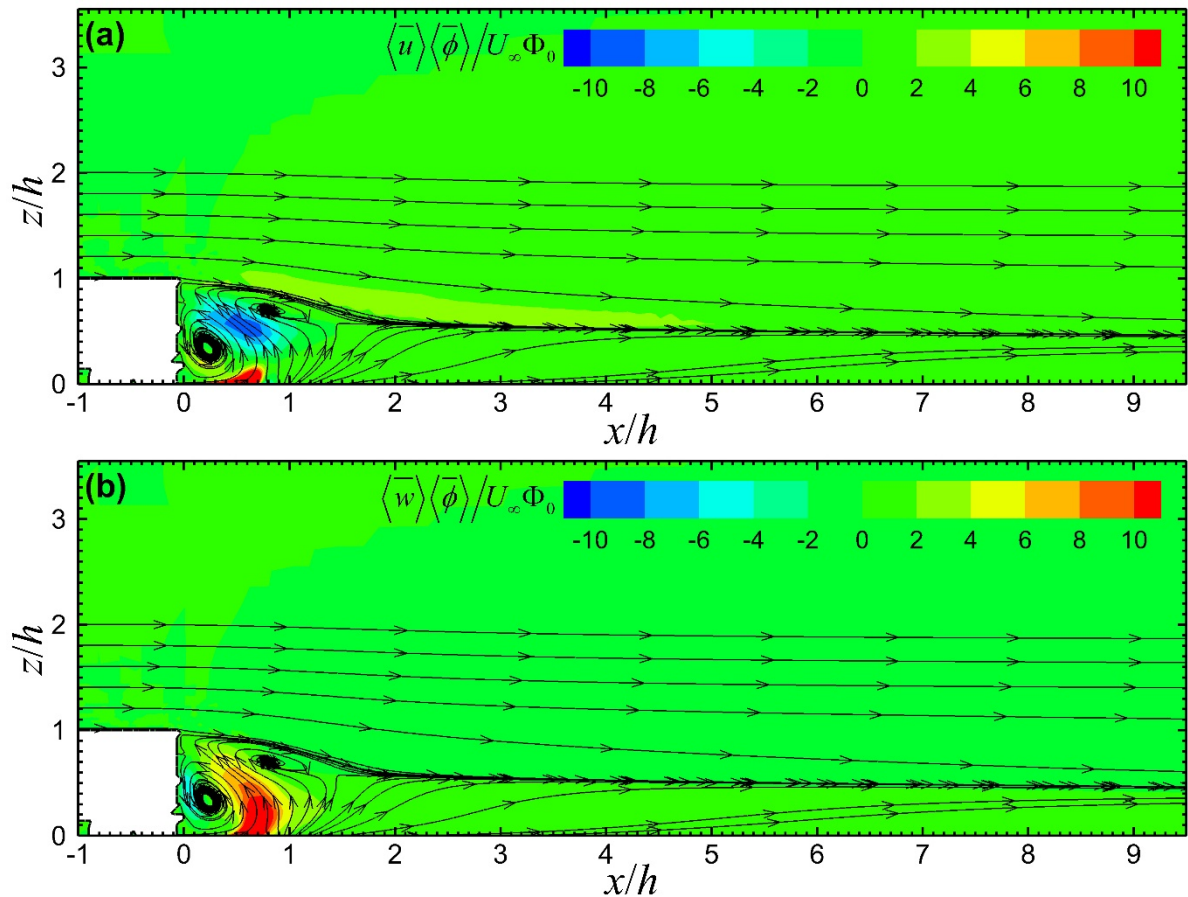


Figure 12. Shaded contours of dimensionless (a). streamwise $\langle \bar{u} \rangle \langle \bar{\phi} \rangle / U_\infty \Phi_0$ and (b) vertical $\langle \bar{w} \rangle \langle \bar{\phi} \rangle / U_\infty \Phi_0$ mean pollutant fluxes on the vertical (x - z) centre plane at $y = 0$. Also shown are the streamlines.

390

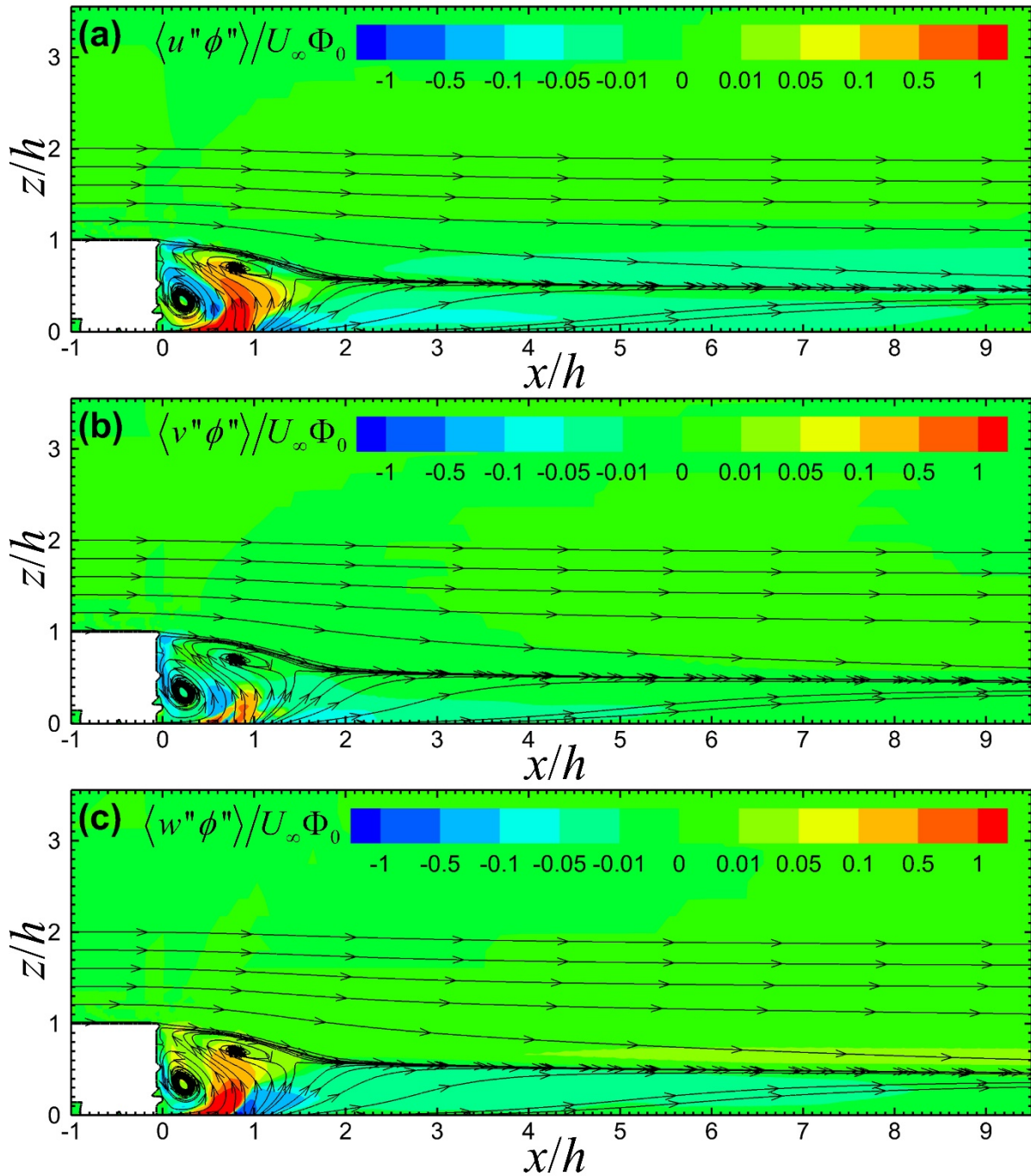


Figure 13. Shaded contours of dimensionless (a). streamwise $\langle \phi' u' \rangle / U_\infty \Phi_0$, (b). spanwise $\langle \phi' v' \rangle / U_\infty \Phi_0$ and (c). vertical $\langle \phi' w' \rangle / U_\infty \Phi_0$ turbulent pollutant fluxes on the vertical (x - z) centre plane at $y = 0$. Also shown are the streamlines.

391

392 The turbulent pollutant fluxes $\langle \phi' u_i' \rangle$ are largely negative within the major
 393 recirculation (Figure 13) that signify the rapid dilution by mean flows. Their magnitudes
 394 ($|\langle \phi' u_i' \rangle| \approx U_\infty \Phi_0$) are much smaller than those of mean pollutant fluxes ($|\langle \bar{u}_i \rangle \langle \bar{\phi} \rangle| \approx 10 U_\infty$
 395 Φ_0). Hence, the early plume mixing is fast and homogeneous that is dominated by the mean
 396 pollutant fluxes.

397

398 A broad maximum of streamwise turbulent pollutant flux $\langle \phi' u' \rangle = U_\infty \Phi_0$ is found in
 399 $0.5 \leq x/h \leq 1$. It is positive across the streamlines that suggests the majority turbulent pollutant
 400 removal from the major recirculation in the streamwise direction to the upper recirculation and
 401 to the far field (Figure 13a). The near-ground negative streamwise turbulent pollutant flux
 402 ($\langle \phi' u' \rangle = -0.5 U_\infty \Phi_0$) for $x \geq h$, on the other hand, depicts the pollutant dilution by the
 403 prevailing flows. Another region of negative streamwise turbulent pollutant flux ($\langle \phi' u' \rangle = -$
 404 $0.5 U_\infty \Phi_0$) is developed within the major recirculation. The spanwise pollutant flux $\langle \phi' v' \rangle =$
 405 $-0.1 U_\infty \Phi_0$ is also negative for $x \geq h$ (Figure 13b). Both the streamwise and spanwise turbulent
 406 pollutant fluxes diminish for $x \geq 5h$. Small amounts of positive (upward) and negative
 407 (downward) vertical turbulent pollutant fluxes ($\langle \phi' w' \rangle = \pm 0.05 \Phi_0 U_\infty$) are found over and
 408 below the flow convergence, respectively (Figure 13c). These findings in turn suggest the
 409 crosswind pollutant transport in the far field which are analogous to those of Gaussian plume
 410 model along the plume trajectory. The far-field vehicular plume thus gradually resumes the
 411 Gaussian form. The vertical turbulent pollutant flux $\langle \phi' w' \rangle = -0.5 U_\infty \Phi_0$ is also negative for

412 $x \approx h$ near the ground (Figure 13c) that is attributed to the dilution along ascending flows. It is
 413 positive along the major recirculation that indicates the turbulent pollutant transport from the
 414 major recirculation to the upper recirculation then the upper shear layer.

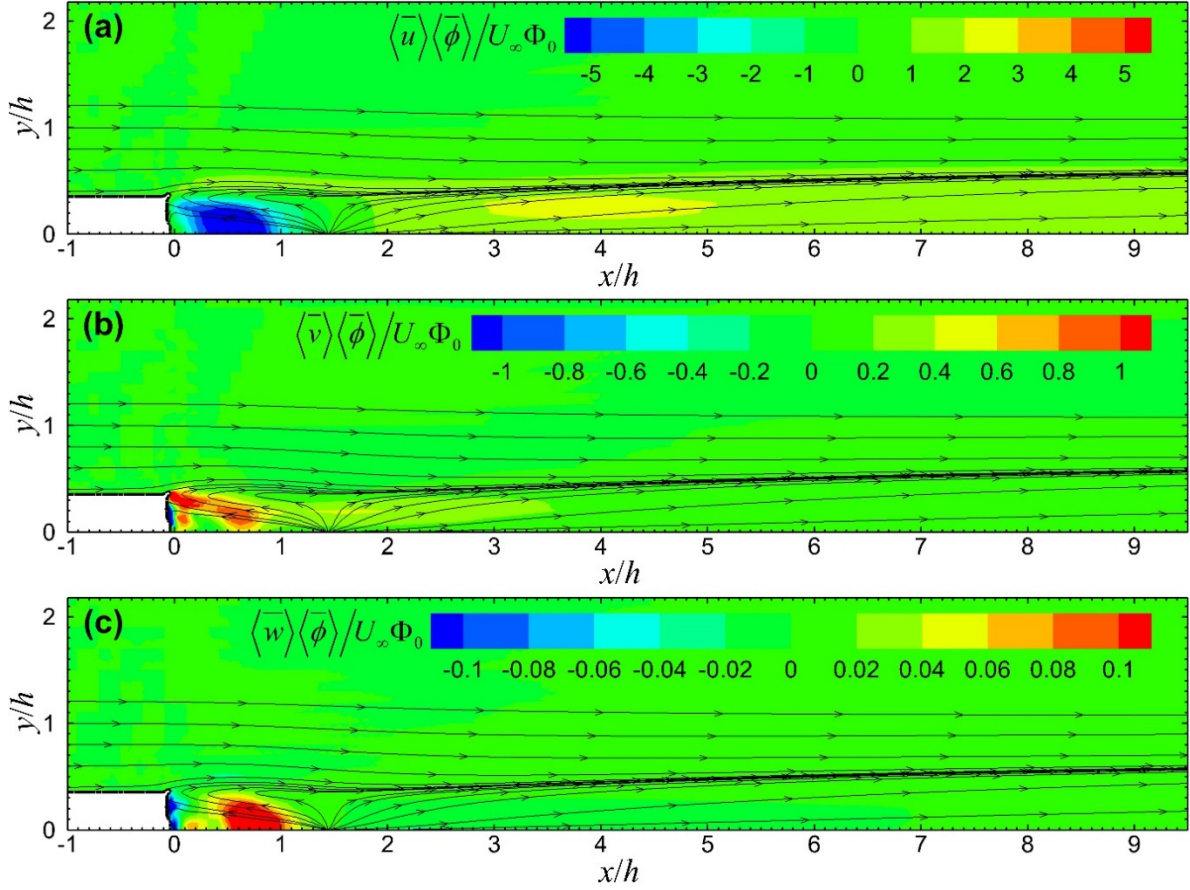


Figure 14. Shaded contours of dimensionless (a). streamwise $\langle \bar{u} \rangle \langle \bar{\phi} \rangle / U_\infty \Phi_0$, (b) spanwise $\langle \bar{v} \rangle \langle \bar{\phi} \rangle / U_\infty \Phi_0$ and (c). vertical $\langle \bar{w} \rangle \langle \bar{\phi} \rangle / U_\infty \Phi_0$ mean pollutant fluxes on the horizontal (x - y) plane at $z = 0.5h$. Also shown are the streamlines.

415

416 On the horizontal (x - y) plane at $z = h/2$ (Figure 14a), the streamwise mean pollutant
 417 flux is negative ($\langle \bar{\phi} \rangle \langle \bar{u} \rangle = -5\Phi_0 U_\infty$) and positive ($\langle \bar{\phi} \rangle \langle \bar{u} \rangle \geq \Phi_0 U_\infty$), respectively, in the major
 418 recirculation (reverse pollutant transport) and the far field (pollutant advection downstream).
 419 In particular, there is a local maximum $\langle \bar{\phi} \rangle \langle \bar{u} \rangle = 3\Phi_0 U_\infty$ at $x = 4h, y = 0.3h$ that is in line with
 420 the off-centre local maximum pollutant concentration presented before (Figure 10). Slightly
 421 elevated streamwise mean pollutant flux ($\langle \bar{\phi} \rangle \langle \bar{u} \rangle = 2\Phi_0 U_\infty$) is shown along the flow

422 convergence because of the high speeds in the shear layer. On the other hand, the spanwise
 423 mean pollutant flux ($\langle \bar{\phi} \rangle \langle \bar{v} \rangle \geq 0.8\Phi_0 U_\infty$) is almost all positive (except very close to the trunk)
 424 that widens the plume coverage (Figure 14b). Unlike its streamwise counterpart, the spanwise
 425 mean pollutant flux diminishes for $x \geq 5h$ even overlapping with the dividing streamlines. The
 426 flows largely resume to the prevailing ones so the spanwise velocity is minimal. Within the
 427 major recirculation, positive vertical mean pollutant flux $\langle \bar{\phi} \rangle \langle \bar{w} \rangle = 0.1\Phi_0 U_\infty$ is shown in $0.5h \leq$
 428 $x \leq h$ and negative $\langle \bar{\phi} \rangle \langle \bar{w} \rangle = -0.1\Phi_0 U_\infty$ is limited to the trunk base (Figure 14c). After the major
 429 recirculation, the vertical mean pollutant flux diminishes due to the prevailing horizontal flows.
 430 The far-field vertical pollutant transport is thus dominated by turbulence as discussed above in
 431 Figure 13. The extremities inside the major recirculation further support the reverse pollutant
 432 transport by advection toward the trunk.

433

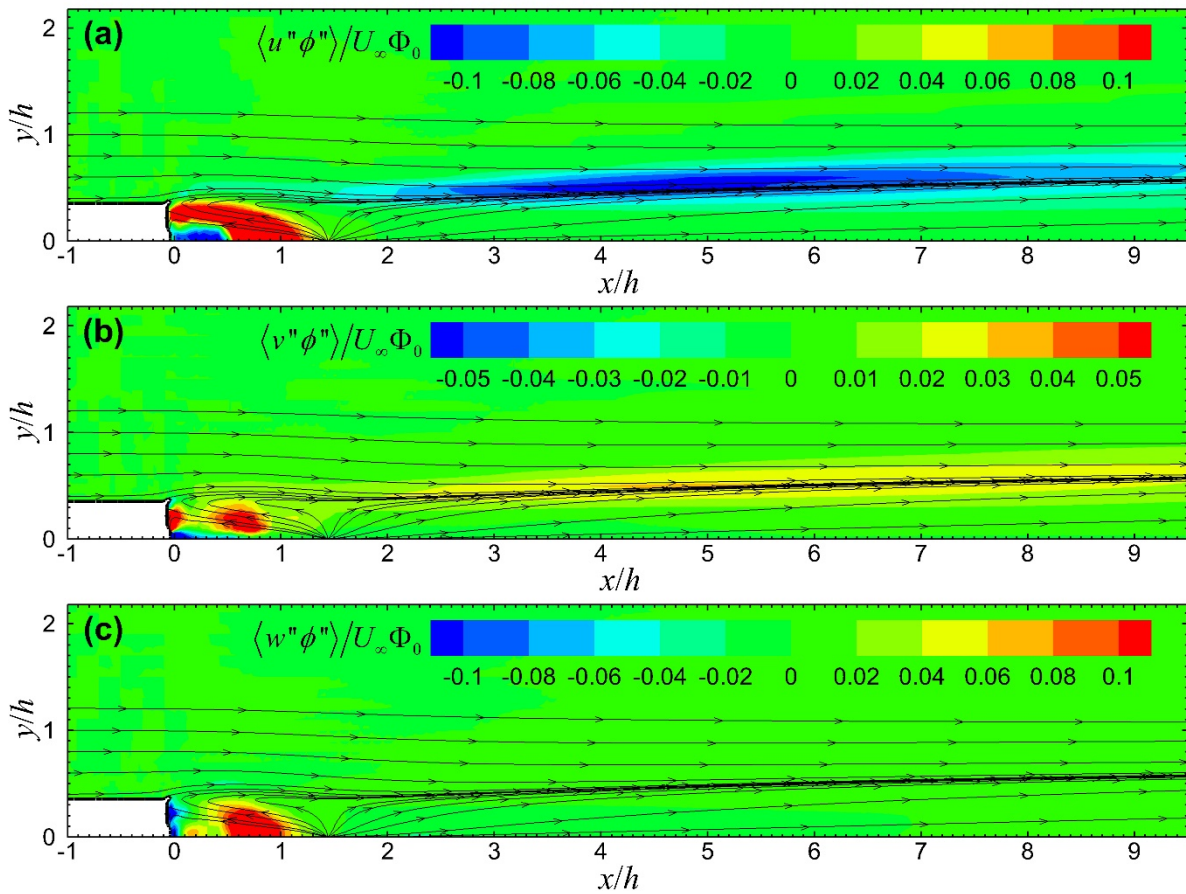


Figure 15. Shaded contours of dimensionless (a). streamwise $\langle \phi' u' \rangle / U_\infty \Phi_0$, (b) spanwise $\langle \phi' v' \rangle / U_\infty \Phi_0$ and (c). vertical $\langle \phi' w' \rangle / U_\infty \Phi_0$ turbulent pollutant fluxes on the horizontal (x - y) plane at $z = h/2$. Also shown are the streamlines.

434

435 The turbulent pollutant fluxes $\langle \phi' u_i' \rangle$ on the horizontal (x - y) plane at $z = h/2$ concur
 436 the mixing processes inside the major recirculation (Figure 15). The spanwise turbulent
 437 pollutant flux is smaller than the other two components (by 50%) because the major
 438 recirculation is rotating about the spanwise (y) axis. Within the near wake, the streamwise
 439 turbulent pollutant flux is largely positive which overlaps with the streamlines of reverse flows
 440 (dilution by advection). Only a tiny negative region is found close to the symmetry plane. In
 441 the far field, a prolonged local minimum of streamwise turbulent pollutant flux ($\langle \phi' u' \rangle \leq -$
 442 $0.04\Phi_0 U_\infty$) overlaps with the flow convergence (Figure 15a). This finding is in line with the
 443 elevated streamwise fluctuating velocity ($\langle u' u' \rangle^{1/2} = 0.1 U_\infty$) reported before in Figure 8a so
 444 the pollutant is diluted rapidly by the prevailing flows. Turbulent transport, on the other hand,
 445 are illustrated clearly by the local maxima of spanwise turbulence pollutant flux $\langle \phi' v' \rangle =$
 446 $0.05\Phi_0 U_\infty$ across the streamlines at $x = 0.5h$ (Figure 15b) that carries the pollutant out of the
 447 major recirculation. Another elongated local maximum $\langle \phi' v' \rangle = 0.04\Phi_0 U_\infty$ is observed in the
 448 far field that transports the pollutant across the flow convergence by turbulence as well. Its
 449 function is similar to that of Gaussian plume. The vertical turbulent pollutant flux has a
 450 distribution alike its mean component (Figure 14c). It gradually diminishes in the far field
 451 because of the prevailing flows (Figure 15c).

452

453 4. Discussion

454 The dynamics and transport mechanism discussed above facilitate our interpretation of
 455 tailpipe dispersion after an on-road vehicle. The distribution of mean pollutant concentration

456 $\langle \bar{\phi} \rangle$ after a fast-back, heavy-duty truck is quite different from that calculated by the Gaussian
457 models. Within the major recirculation, the tailpipe emission is homogeneously mixed that
458 results in a rather uniform mean pollutant concentration. Instead of an infinitely small pollutant
459 point source, the size of the major recirculation is comparable to the height of trunk h . Under
460 this circumstance, the conventional Gaussian models are no longer applicable to the near-wake
461 dispersion calculation. Besides, turbulent transport is required to move the pollutant from the
462 major recirculation to the far field. The pollutant concentration drops sharply in the streamwise
463 direction and a noticeable concentration gradient is developed in-between.

464

465 After the major recirculation, the flows gradually resume to the prevailing ones so the
466 Gaussian models are applicable. It is noteworthy that tailpipe emission is driven to a higher
467 level ($z = h/2$) in the major recirculation before being removed to the upper recirculation and
468 the far field. The plume trajectory is escalated but not at the tailpipe level so the emission height
469 should be adjusted accordingly for $x \geq h$. The horizontal, crosswind plume dispersion also
470 differs from the Gaussian theory. In view of the trailing vortices, the maximum pollutant
471 concentration is not along the centreline but shifts sideward to $y \approx 0.3h$. The peaks of fluctuating
472 pollutant concentration are shifted as well.

473

474 The above findings help refine the practice of remote sensing. We reported that a long
475 sampling duration is unfavourable to remote sensing accuracy (Huang et al. 2020). The
476 different diffusion coefficients of nitric oxide (NO) and carbon dioxide (CO₂) in air lead to
477 different dispersion patterns so that the NO/CO₂ ratio (the only parameter that is measured in
478 remote sensing) is constant only in a short distance after the tailpipe exit and then reduces
479 further downstream.

480

481 The aerodynamics after a heavy-duty truck reported in this paper shed some light on
 482 the reliable range of remote sensing (short sampling duration) as well. The LES results show
 483 that the major recirculation is enclosed by dividing streamlines. The pollutant removal from
 484 the major recirculation to the far field is governed by turbulent pollutant fluxes $\langle \phi'' u_i'' \rangle$
 485 (across the streamlines), which, however, are much weaker (about an order of magnitude) than
 486 the mean pollutant flux $\langle \bar{\phi} \rangle \langle \bar{u}_i \rangle$. A noticeable difference in pollutant concentration is therefore
 487 developed. Despite the chemical composition, the pollutant concentrations drop sharply after
 488 the near wake (an order of magnitude). A long sampling duration would be prone to
 489 underestimating the tailpipe emission. Besides, the sharp drop in pollutant concentrations
 490 demands a higher detection sensitivity, which might stretch the capability of remote sensing to
 491 the limit. (Could Yuhan please comment on the revision?) It in turn adversely affects the signal
 492 collected and measurement accuracy. The far-field plume trajectory is escalated from the
 493 tailpipe to a higher level ($z \approx h/2$) which is unfavourable to sampling confidence (could it be
 494 made more precise in its meaning?).

495

496 According to the above analysis, the best sampling range should be within the major
 497 recirculation ($\leq h$) within which the pollutant mixing is more homogeneous and the
 498 concentration is more uniform. The corresponding sampling duration is therefore $\leq h/U_\infty$. For
 499 example, given an on-road truck of size 3 m at speed 30 km hr⁻¹, the sampling duration should
 500 be less than 0.4 sec. The current practice of remote sensing (0.5 sec) is marginally acceptable.
 501 The sampling time would be shorter for smaller vehicles (e.g. light-duty lorry) and faster
 502 driving speeds (e.g. 80 km hr⁻¹ on most of the highways in Hong Kong). Apparently, slower
 503 driving speed would help improve the remote sensing accuracy. Otherwise, a shorter sampling
 504 duration is more favourable.

505

506 There exists another technical difficulty for shorter sampling duration. Unlike the usual
 507 turbulence intensities (approximately 10%), the current LES unveils that the fluctuating
 508 pollutant concentrations is up to 20% of the mean pollutant concentration in the major
 509 recirculation ($\langle \phi' \phi' \rangle^{1/2} = 0.2 \langle \bar{\phi} \rangle$). It is thus expected that the signal data are noisy such that
 510 the conventional turbulence measurements should be implemented cautiously. One of the
 511 solutions could be prolonged sampling time, which, however, is unlikely practicable in remote
 512 sensing.

513

514 **5. Conclusion**

515 In this study, the flow and dispersion after an on-road heavy-duty truck are examined
 516 by LES in detail. The currently LES results agree well with our previous wind tunnel
 517 visualization and the wind profiles available in the literature. In line with previous studies, the
 518 flows after a fast-back truck can be divided into the near-wake and far-field regions. The near
 519 wake is composed of the major recirculation and the upper recirculation while the far field
 520 mainly consists of two trailing vortices. The upper shear layer not only induces the upper
 521 recirculation but also modifies the flows in the trailing vortices. It entrains into the trailing
 522 vortices finally.

523

524 Tailpipe emission is carried towards the truck following the major recirculation (reverse
 525 flows). Simultaneously, the pollutants are escalated from the tailpipe to a high level ($z \approx h/2$).
 526 In view of the rapid mixing, the pollutants are more homogeneous and the concentrations are
 527 more uniform within the major recirculation. In the far-field, the pollutant transport gradually
 528 follows the conventional Gaussian theory. However, the pollutant concentration is not peaked
 529 at the symmetric plane $y = 0$ but shifted sideward to $y = 0.3h$. Interestingly, substantially
 530 turbulent transport is found across those dividing streamlines. Generally, the transport by

531 pollutant advection is about 10 times larger than that by turbulence. It thus explains the
532 thorough mixing in the major recirculation.

533

534 The current LES complements our previous findings such that a shorter sampling
535 duration favours remote sensing accuracy. In this paper, it is proposed that the sampling
536 coverage should not extend beyond the major recirculation. Otherwise, the remote sensing
537 signal would underestimate the pollutant concentrations. Nonetheless, the sampling time (0.5
538 sec) adopted in remote sensing nowadays is marginally acceptable.

539

540 Turbulence, especially within the shear layers from two sides of the truck and the region
541 directly behind the recirculation, disperses the pollutant outside the recirculation. The trailing
542 vortices can further elevate the pollutant to the level of around $z = 0.5h$ and the upper shear
543 layer suppresses pollutant from being driven to a higher level. Most pollutant in the far field is
544 trapped and transported downstream by the trailing vortices, while turbulence induced by the
545 upper shear layer and trailing vortices can disperse the pollutant within the vortices upwards
546 and downwards, separately. The strong turbulence in the region between trailing vortices and
547 mean flow also transports pollutant spanwise. Moreover, the turbulence induced by the trailing
548 vortices leads to reverse pollutant dispersion back to the truck, which opposes the prevailing
549 flows. These findings collectively formulate the pollutant dispersion mechanisms behind an
550 on-road truck as well as help pedestrians prevent from the harmful effects of vehicular emission.

551

552 **Acknowledgment**

553 This research is conducted in part using the research computing facilities and/or
554 advisory services offered by Information Technology Services (ITS), The University of Hong
555 Kong (HKU). Technical support from Ms. Lilian Y.L. Chan, Mr. W.K. Kwan and Mr. Bill H.T.

556 Yau is appreciated. This work was supported by the Environmental and Conservation Fund
557 (ECF) Project 26/2018 of the Hong Kong (HK) SAR.

558

559

560

561 **References**

562 Ahmed, S.R. (1981), “An experimental study of the wake structures of typical automobile
563 shapes”, *J. Wind Eng. Ind. Aerod.* **9**, 49-62.

564 Ahmed, S.R., Gawthorpe, R.G. and Mackrodt, P.A. (1985), “Aerodynamics of road and rail
565 vehicles”, *Veh. Syst. Dyn.* **14**, 319–92.

566 Anenberg, S.C., Miller, J., Minjares, R., Du, L., Henze, D.K., Lacey, F., Malley, C.S.,
567 Emberson, L., Franco, V., Klimont, Z. and Heyes, C. (2017), “Impacts and mitigation
568 of excess diesel-related NO_x emissions in 11 major vehicle markets”, *Nature* **545**, 467–
569 471.

570 Baker, C.J. (2001), “Flow and dispersion in ground vehicle wakes”, *J. Fluids Struct.* **15**, 1031-
571 1060.

572 Benson, P.E. (1992), “A review of the development and application of the CALINE3 and 4
573 models”, *Atmos. Environ. Part B. Urban Atmosphere* **26**, 379-390.

574 Berkowicz, R. (2000), “OSPM - A parameterised street pollution model”, *Environ. Monit.*
575 *Assess.* **65**, 323-331.

576 Cadle, S.H. and Stephens, R.D. (1994), “Remote sensing of vehicle exhaust emissions”,
577 *Environ. Sci. Technol.* **28**, 258-264.

578 Carpentieri, M., Kumar, P. and Robins, A. (2012), “Wind tunnel measurements for dispersion
579 modelling of vehicle wakes”, *Atmos. Environ.* **62**, 9-25.

- 580 Chan, T.L., Dong, G., Cheung, C.S., Leung, C.W., Wong, C.P. and Hung, W.T. (2001), “Monte
581 Carlo simulation of nitrogen oxides dispersion from a vehicular exhaust plume and its
582 sensitivity studies”, *Atmos. Environ.* **35**, 6117-6127.
- 583 Chan, T.L., Luo, D.D. Cheung, C.S. and Chan, C.K. (2008), “Large eddy simulation of flow
584 structures and pollutant dispersion in the near-wake region of the studied ground
585 vehicle for different driving conditions”, *Atmos. Environ.* **42**, 5317-5339.
- 586 Chang, V.W.-C., Hildemann, L.M. and Chang, C.-h. (2009a), “Wind tunnel measurements of
587 the dilution of tailpipe emissions downstream of a car, a light-duty truck, and a heavy-
588 duty truck tractor head”, *J. Air & Waste Manage. Assoc.* **59**, 704-714.
- 589 Chang, V.W.-C., Hildemann, L.M. and Chang, C.-h. (2009b), “Dilution rates for tailpipe
590 emissions: Effects of vehicle shape, tailpipe position, and exhaust velocity”, *J. Air &
591 Waste Manage. Assoc.* **59**, 715-724.
- 592 Cheng, W.C. and Liu, C.-H. (2011). Large-eddy simulation of flow and pollutant transports in
593 and above two-dimensional idealized street canyons”, *Boundary-Layer Meteorol.* **139**,
594 411-437.
- 595 Choi, H., Lee, J. and Park, H. (2014), “Aerodynamics of heavy vehicles”, *Annu. Rev. Fluid
596 Mech.* **46**, 441-468.
- 597 Clifford, M.J., Clarke, R. and Riffat, S.B. (1997), “Local aspects of vehicular pollution”, *Atmos.
598 Environ.* **31**, 271-276.
- 599 Dong, G. and Chan, T.L. (2006), “Large eddy simulation of flow structures and pollutant
600 dispersion in the nearwake region of a light-duty diesel vehicle”, *Atmos. Environ.* **40**,
601 1104-1116.
- 602 Gosse, K., Paranthoën, P., Patte-Rouland, B. and Gonzalez, M. (2006), “Dispersion in the near
603 wake of idealized car model”, *Int. J. Heat Mass Tran.* **49**, 1747-1752.

- 604 Gosse, K., Gonzalez, M., and Paranthoën, P. (2011). “Mixing in the three-dimensional wake
605 of an experimental modelled vehicle”, *Environ. Fluid Mech.* **11**, 573-589.
- 606 Habegger, L.J., Wolsko, T.D., Camaioni, J.E., Kellermeyer, D.A. and Dautzvardis, P.A. (1974),
607 *Dispersion Simulation Techniques for Assessing the Air Pollution Impacts of Ground*
608 *Transportation Systems*, Energy and Environmental Systems Division, Argonne
609 National Laboratory, Illinois 60439.
- 610 Hu, X.J., Yang, H.B., Yang, B., Li, X.C. and Lei, Y.L. (2015), “Effect of car rear shape on
611 pollution dispersion in near wake region”, *Math. Probl. Eng.* **2015**, 879735.
- 612 Huang, Y., Organa, B., Zhou, J.L., Surawska, N.C., Hong, G., Chan, E.F.C. and Yam, Y.S.
613 (2018), “Remote sensing of on-road vehicle emissions: Mechanism, applications and a
614 case study from Hong Kong”, *Atmos. Environ.* **182**, 58-74.
- 615 Huang, Y., Ng, E.C.Y., Surawski, N.C., Yam, Y.-S., Mok, W.-C., Liu, C.-H., Zhou, J.L., Organ,
616 B. and Chan, E.F.C. (2020), “Large eddy simulation of vehicle emissions dispersion:
617 Implications for on-road remote sensing measurements”, *Environ. Pollut.* **259**, 113974.
- 618 Hucho, W.-H., (1987), *Aerodynamics of Road Vehicles: From Fluid Mechanics to Vehicle*
619 *Engineering*, 4th Edition, SAE International, Warrendale, USA, 956 pp.
- 620 Kanda, I., Uehara, K., Yamao, Y., Yoshikawa, Y. and Morikawa, T. (2006), “A wind-tunnel
621 study on exhaust gas dispersion from road vehicles—Part I: Velocity and concentration
622 fields behind single vehicles”, *J. Wind Eng. Ind. Aerod.* **94**, 639-658.
- 623 Kota, S.H., Ying, Q. and Zhang, Y. (2013), “Simulating near-road reactive dispersion of
624 gaseous air pollutants using a three-dimensional Eulerian model”, *Sci. Total Environ.*
625 **454**, 348-357.
- 626 Lesieur, M., Métais, O. and Comte, P. (2018), *Large-Eddy Simulations of Turbulence*,
627 Cambridge University Press, Cambridge, United Kingdom.

- 628 Liu, C.-H., Xie, J., Huang, Y. and Mok, W.-c. (2019), “Near-field vehicular plume mixing and
629 roadside air quality”, *The 15th International Conference on Wind Engineering*
630 *(ICWE15)*, September 1 to 6, 2019, Beijing, China.
- 631 Lo, K.H. and Kontis, K. (2017), “Flow around an articulated lorry model”, *Exp. Therm. Fluid*
632 *Sci.* **82**, 58-74.
- 633 McArthur, D., Burton, D., Thompson, M. and Sheridan, J. (2016), “On the near wake of a
634 simplified heavy vehicle”, *J. Fluids Struct.* **66**, 293-314.
- 635 Minguéz, M., Pasquetti, R. and Serre, E. (2008), “High-order large-eddy simulation of flow
636 over the “Ahmed body” car model”, *Phys. Fluids* **20**, 095101.
- 637 Ning, Z., Cheung, C.S., Lu, Y., Liu, M.A. and Hung, W.T. (2005). “Experimental and
638 numerical study of the dispersion of motor vehicle pollutants under idle condition”,
639 *Atmos. Environ.* **39**, 7880-7893.
- 640 Owais, M. (2019), “Location strategy for traffic emission remote sensing monitors to capture
641 the violated emissions”, *J. Adv. Transport.* **2019**, 6520818.
- 642 Pospisil, J., Katolicky, J. and Jicha, M. (2004), “A comparison of measurements and CFD
643 model predictions for pollutant dispersion in cities”, *Sci. Total Environ.* **334**, 185-195.
- 644 Rao, S.T. and Keenan, M.T. (1980), “Suggestions for improvement of the EPA-HIWAY
645 model”, *J. Air & Waste Manage. Assoc.* **30**, 247-256.
- 646 Rohit, R., Kini, C.R. and Srinivas, G. (2019), “Recent trends in aerodynamic performance
647 developments of automobile vehicles: a review”, *Journal of Mechanical Engineering*
648 *Research and Developments*, **42**, 206-214.
- 649 Sellappan, P., McNally, J. and Alvi1, F.S. (2018), “Time-averaged three-dimensional flow
650 topology in the wake of a simplified car model using volumetric PIV”, *Exp. Fluids* **59**,
651 124.

- 652 Tunay, T., Yaniktepe, B. and Sahin, B. (2016), “Computational and experimental
653 investigations of the vortical flow structures in the near wake region downstream of the
654 Ahmed vehicle model”, *J. Wind Eng. Ind. Aerod.* **159**, 48-64.
- 655 Vio, G., Watkins, S., Mousley, P., Watmuff, J. and Prasad, S. (2005), “Flow structures in the
656 near-wake of the Ahmed model”, *J. Fluids Struct.* **20**, 673–695.
- 657 Wang, X.W., Zhou, Y., Pin, Y.F. and Chan, T.L. (2013), “Turbulent near wake of an Ahmed
658 vehicle model”, *Exp. Fluids* **54**, 1490.
- 659 Wang, Y.J., Nguyen, M.T., Steffens, J.T., Tong, Z., Wang, Y., Hopke, P.K. and Zhang, K.M.
660 (2013), “Modeling multi-scale aerosol dynamics and micro-environmental air quality
661 near a large highway intersection using the CTAG model”, *Sci. Total Environ.* **443**,
662 375-386.
- 663 Weller, H.G., Tabor, H., Jasak, H. and Fureby, C. (1998), “A tensorial approach to
664 computational continuum mechanics using object-oriented techniques”, *Comput. Phys.*
665 **12**, 620-631.
- 666 Xie, S., Bluett, J., Fisher, G. and Kuschel, G. (2004), “On-road remote sensing identifies the
667 worst vehicle polluters”, *Water & Atmosphere* **12**, 8-9.
- 668 Xing, Y. and Brimblecombe, P. (2018), “Dispersion of traffic derived air pollutants into urban
669 parks”, *Sci. Total Environ.* **622**, 576-583.
- 670 Zhao, Y., Kato, S. and Zhao, J. (2015), “Numerical analysis of particle dispersion
671 characteristics at the near region of vehicles in a residential underground parking lot”,
672 *J. Disper. Sci. Technol.* **36**, 1327-1338.
- 673 Zhang, K. and Batterman, S. (2013), “Air pollution and health risks due to vehicle traffic”, *Sci.*
674 *Total Environ.* **450**, 307-316.
- 675 Zhang, B.F., Zhou, Y. and To, S. (2015), “Unsteady flow structures around a high-drag Ahmed
676 body”, *J. Fluid Mech.* **777**, 291-326.